Enhancement of a 2D front-tracking algorithm with a non-uniform distribution of Lagrangian markers

Mijail Febres, Dominique Legendre *

Institut de Mécanique des Fluides de Toulouse (IMFT) – Université de Toulouse, CNRS-INPT-UPS, Toulouse, France

A B S T R A C T

The 2D front tracking method is enhanced to control the development of spurious velocities for non-uniform distributions of markers. The hybrid formulation of Shin et al. (2005) [7] is considered. A new tangent calculation is proposed for the calculation of the tension force at markers. A new reconstruction method is also proposed to manage non-uniform distributions of markers. We show that for both the static and the translating spherical drop test case the spurious currents are reduced to the machine precision. We also show that the ratio of the Lagrangian grid size Δs over the Eulerian grid size Δx has to satisfy $\Delta s/\Delta x > 0.2$ for ensuring such low level of spurious velocity. The method is found to provide very good agreement with benchmark test cases from the literature.

1. Introduction

Numerical simulations of two-phase flows requires the resolution of moving/deforming fluid interfaces. Among the methods reported in the literature, the front-tracking method presents itself as a promising alternative. One of the main advantages of the front-tracking method for the treatment of interfaces is that the surface tension contribution can be simplified. Indeed, instead of calculating a local curvature as seen in volume-tracking methods like VOF [1–3] or Level Set [4–6], the surface tension contribution in the front-tracking method is determined through the calculation of tangential forces on the edges (or the nodes in 2D) of surface elements [7]. This ensures that the total force on any closed surface is zero, which is beneficial in long simulations [8,7]. This advantage comes with some shortcomings. Fluid interfaces can move and deform in such a way that markers forming the front can travel in the tangential direction to the interface, accumulating in small interface areas, or leaving large interface areas without any markers. This is shown in Fig. 1(a), where a rising bubble is simulated on a uniform Eulerian grid of cell size Δx and the interface is initialized with front elements of size $\Delta s = \Delta x$. A loss of precision is observed when the density of marker is reduced but instabilities can be observed when the number of markers is increased [9,10] (see Fig. 1(b)). Adding or removing elements from the front according to some threshold of element size Δs is a relatively simple procedure [11,12]. However, it is not clear how the flow is then affected, and algorithmic complexity is expected in interface merging and break-up problems, as well as in 3D calculations. Controlling an uniform distribution of markers works well enough in cases involving interfaces with moderate deformation [see for example the work of [13], where an artificial tangential marker velocity is applied], but some perturbations can be observed on the bubble sides as shown in Fig. 2(a). A similar behavior is expected when instead of using an artificial velocity, polynomials/functions are fitted to the markers and are used to keep a uniform distribution of the front [14,15]. Also, markers can suffer small amplitude mesh-scale oscillations that are not physical [14]. The application of smoothing

* Corresponding author.
E-mail address: legendre@imft.fr (D. Legendre).

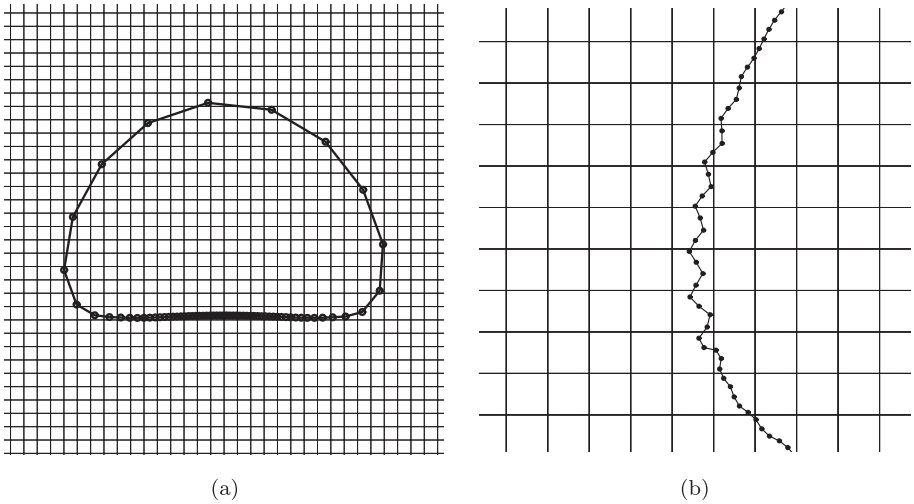

Fig. 1. Front-tracking method implemented in JADIM (present work, without any reconstruction/redistribution), applied to a rising Bubble with $\rho_1/\rho_2 = 10$, $\mu_1/\mu_2 = 10$, $\sigma = 24.5$, $g = 0.98$, $Re = 35$, $Eo = 10$ [following [17]]. (a) Bubble shape with the use of 63 markers. (b) Zoom on the left side of the bubble when increasing $\times 4$ the number of markers.

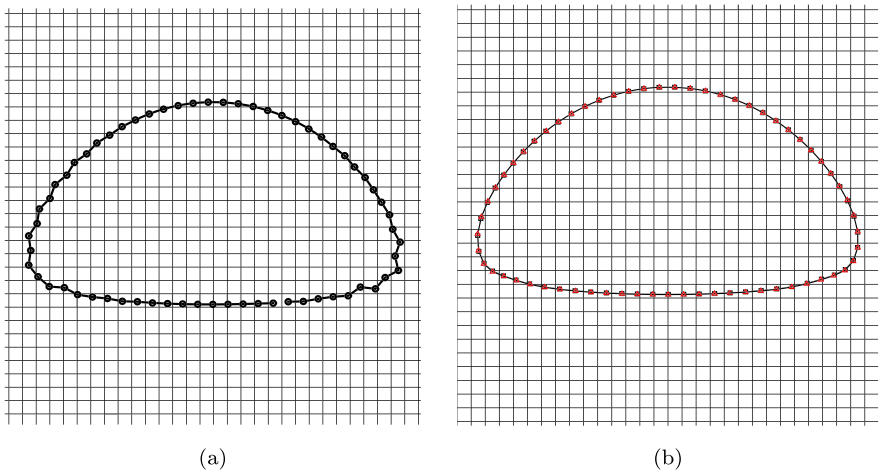

Fig. 2. Bubble case shown in Fig. 1(a) using 63 front markers treated with: (a) Artificial tangential marker velocity. (b) Artificial tangential marker velocity combined with: ▲ Fourth order filter [14]; ◘ Savitzki–Golay [16] filter.

filters [14,16], seems to alleviate this effect. The combination of both artificial tangential marker velocity and smoothing filter allows to recover a relevant bubble shape as shown in Fig. 2(b). These treatments that seem to solve the front-tracking method issues were developed in the context of uniform distributions of markers and their extension to 3D problems is not obvious.

Shin et al. [7] introduced a "hybrid formulation" treatment for the surface tension contribution and reported a reduction of spurious velocities down to machine precision for an uniform distribution of markers. They also proposed a reconstruction method based on an optimum indicator function contour to obtain a mass-conservative method for non-uniform marker distributions. This approach was reported to be robust enough to solve all the issues described above. However, their reconstruction method produces a non-uniform distribution of markers which affects negatively the ability of the "Hybrid formulation" to reduce spurious velocities.

The objective of this work is to propose a new method for the calculation of the tangents used in the capillary contribution that guaranties the reduction of spurious velocities to machine precision even for a non-uniform distribution of markers. We also propose a new front reconstruction method that remarkably preserves the spurious currents reduction of the hybrid formulation close to machine precision. The present work is organized as follows. In section 2 we describe the numerical implementation of the front-tracking method inside the in-house code JADIM, giving emphasis in section 3 to both the new approach for the calculation of the tangents and the new method for the front reconstruction. In section 4, we validate the new approach for the calculation of the tangents using classic spurious velocity tests from the literature: we consider the static and translating 2D drop test cases and we analyze the effect of the Laplace number, the Capillary

number, the grid refinement and the time step on the spurious velocity development. In section 5, we validate the new reconstruction method using the same test cases and also considering the oscillating drop test case. We test the whole implementation against 2D rising bubble benchmarks in section 6.

2. Numerical method

2.1. General solver

For this study, we use the in-house code JADIM, developed at IMFT. The treatment of moving interfaces in JADIM has been detailed in the literature [18–22]. Considering two Newtonian incompressible isothermal fluids, no mass transfer at the interface and a constant surface tension, the following 1-fluid formulation for the Navier–Stokes equations writes:

$$\nabla \cdot \boldsymbol{U} = 0 \tag{1}$$

$$\frac{\partial \boldsymbol{U}}{\partial t} + (\boldsymbol{U} \cdot \nabla)\boldsymbol{U} = -\frac{1}{\rho}\nabla P + \frac{1}{\rho}\nabla \cdot \boldsymbol{\Sigma} + \boldsymbol{g} + \boldsymbol{F_\sigma} \tag{2}$$

where $\boldsymbol{U}$ stands for the velocity field, P for the pressure field, $\boldsymbol{\Sigma}$ is the viscous stress tensor, $\boldsymbol{g}$ is the acceleration due to gravity, $\boldsymbol{F}_\sigma$ is the capillary contribution, ρ and μ are the local density and dynamic viscosity, which are calculated using the classical VOF function C ($C = 1$ in fluid 1):

$$\rho = C\rho_1 + (1 - C)\rho_2 \tag{3}$$

$$\mu = C\mu_1 + (1 - C)\mu_2 \tag{4}$$

Equations (1) and (2) are discretized using the finite volume method in a staggered grid and spatial derivatives are calculated using a second-order centered scheme. A third-order three-step Runge–Kutta scheme is used to solve the advective terms time advancement, a semi-implicit Crank–Nicholson method is used to treat viscous terms and a projection method is used to ensure the continuity condition. Besides the *CFL* condition, the time step is selected to satisfy the stability condition imposed by the capillary contribution in the momentum equation [23,24]:

$$\Delta t_{min} < \Delta t_\sigma = \sqrt{\frac{(\rho_1 + \rho_2)\,\Delta x^3}{8\sigma}} \tag{5}$$

2.2. Computing the VoF function C in front-tracking

To calculate C from a given marker distribution, we adopt the procedure found in [15,25]. Briefly, a set of markers identified with indexes k in Fig. 3(a) is distributed along the interface forming the "front" over the Eulerian grid identified with subscripts i, j. Around each front element e of length Δs_e formed by the pair of markers $k-1$ and k, a rectangle (typically B and C in Fig. 3(b)) of width Δs_e and height ℓ can be constructed using the normal unit vector to the element pointing to both sides of the interface. The signed distance to the front is calculated in the cell (i, j) lying inside each rectangle as $|d_{i,j}| = |\boldsymbol{x}_e - \boldsymbol{x_{i,j}}|$ where $\boldsymbol{x_{i,j}}$ is the Eulerian cell centers and $\boldsymbol{x}_e$ is the element center. The sign of $d_{i,j}$ is determined depending on which side of the interface the point $\boldsymbol{x_{i,j}}$ lies. Additionally, irregular quadrilaterals can be constructed for each marker located in between two rectangles on the convex side of the interface (see the quadrilateral A in Fig. 3(b)). They are introduced because regular rectangles will not completely cover convex areas. Inside these irregular quadrilaterals, $d_{i,j}$ is calculated as the distance from the cell center $\boldsymbol{x_{i,j}}$ to the corresponding marker. When a cell center is located in more than one rectangle the minimum distance to the corresponding elements is selected for $d_{i,j}$.

The distance function ϕ to the interface is then determined in each cell (i, j) by:

$$\phi_{i,j} = \begin{cases} -\gamma & \text{if } d_{i,j} < -\gamma, \\ d_{i,j} & \text{if } |d_{i,j}| \leq +\gamma, \\ +\gamma & \text{if } d_{i,j} > +\gamma \end{cases} \tag{6}$$

where γ is the width of band formed by the union of all quadrilaterals, typically $\gamma = 2\sqrt{2}\Delta x$ [see [15]]. The height ℓ of the rectangle is chosen such that $0 < \gamma < \ell$, so the band of width 2γ is contained in the union of all the quadrilaterals constructed before. The calculation of the distance function ϕ is repeated at each time step but only for the cells lying in the vicinity of the interface (given of course that a consistent initialization of ϕ is provided at $t = 0$). It is worth mentioning the simplicity of implementation of ϕ, its accuracy and economy of calculation [see [15,25]].

Once the discrete field for the distance function ϕ is known, the VoF function C is found through the mollified Heaviside function in each cell (i, j):

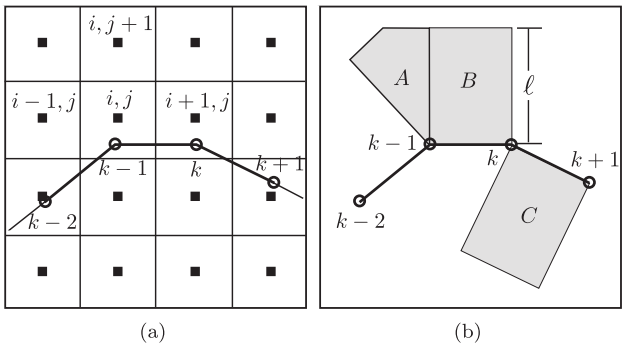

Fig. 3. Front tracking method. (a) Eulerian/Lagrangian grid, showing Eulerian cells i, j and elements formed by Lagrangian markers k; (b) Corresponding quadrilaterals construction used for the calculation of the distance function (for clarity, quadrilaterals on only one side of the front are shown).

$$C_{i,j} = \begin{cases} 0 & \text{if } \phi_{i,j} < -\varepsilon, \\ 0.5\left[1 + \frac{\phi_{i,j}}{\varepsilon} + \frac{1}{\pi}\sin\left(\frac{\pi\phi_{i,j}}{\varepsilon}\right)\right] & \text{if } |\phi_{i,j}| \le \varepsilon, \\ 1 & \text{if } \phi_{i,j} > \varepsilon \end{cases} \tag{7}$$

where $\varepsilon = \sqrt{2}\Delta x$ is approximately half the numerical thickness of the interface.

2.3. Hybrid formulation for the surface tension force

The surface tension force $\boldsymbol{F}_\sigma = \sigma\kappa\boldsymbol{n}\delta$ is calculated following the hybrid formulation introduced by Shin et al. [7]. This method consists in calculating the $\boldsymbol{n}\delta$ contribution on the Eulerian grid while the curvature κ is calculated from the Lagrangian markers. $\boldsymbol{F}_\sigma$ is then calculated as:

$$\boldsymbol{F}_\sigma = -\frac{\sigma}{\rho}\kappa\nabla C \tag{8}$$

Considering for example an $i + 1/2$ face and an $j + 1/2$ face of the staggered grid, the discretization of the capillary force in both direction is then:

$$F_{\sigma\, i+1/2,j} = -\frac{\sigma}{\rho}\,\kappa_{i+1/2,j}\,\frac{C_{i+1,j} - C_{i,j}}{\Delta x} \tag{9}$$

$$F_{\sigma\, i,j+1/2} = -\frac{\sigma}{\rho}\,\kappa_{i,j+1/2}\,\frac{C_{i,j+1} - C_{i,j}}{\Delta y} \tag{10}$$

The calculation of κ is obtained from the capillary force $\boldsymbol{F}'_\sigma$ determined using the makers as follows. We can write $\boldsymbol{F}'_\sigma$ as

$$\boldsymbol{F}'_\sigma = \sigma\kappa\boldsymbol{G} \tag{11}$$

where the discrete numerical expression of $\boldsymbol{F}'_\sigma$ and $\boldsymbol{G}$ onto the Eulerian grid are expressed in the form of a sum over the elements e [7]. For example at an $i + 1/2$ cell face

$$\boldsymbol{F}'_{\sigma\, i+1/2,j} = \sum_e \boldsymbol{f}_e D_{i+1/2,j}(\boldsymbol{x}_e)\Delta s_e \tag{12}$$

$$\boldsymbol{G}_{i+1/2,j} = \sum_e \boldsymbol{n}_e D_{i+1/2,j}(\boldsymbol{x}_e)\Delta s_e \tag{13}$$

where $\boldsymbol{f}_e$ is the capillary force contribution of element e and $D_{i+1/2,j}(\boldsymbol{x}_e)$ is the Dirac distribution function. Their calculation are now detailed.

The local force $\boldsymbol{f}_e$ at a front element e is calculated (in 2D) following [8]:

$$\boldsymbol{f}_e = \int_{\Delta s_e} \sigma\kappa\boldsymbol{n}ds \tag{14}$$

Using the Frenet relation for the curvature of a two-dimensional line, $\kappa\boldsymbol{n} = \partial\boldsymbol{t}/\partial s$, we have:

$$\boldsymbol{f}_e = \sigma\left(\boldsymbol{t}_k - \boldsymbol{t}_{k-1}\right) \tag{15}$$

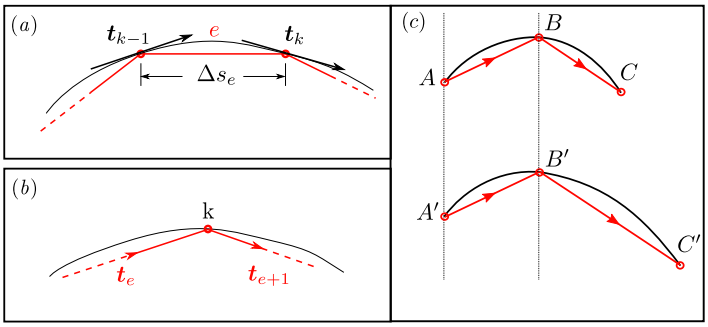

Fig. 4. (*a*) Local force f_e at element e using $\boldsymbol{t}_k$ and $\boldsymbol{t}_{k-1}$ the tangent vectors at markers k and $k-1$ according to equation (15) (present work); (*b*) Local force f_k at marker k using $\boldsymbol{t}_e$ and $\boldsymbol{t}_{e+1}$ the tangents of elements e and $e+1$ according to equation (16). (*c*) Two interfaces defined by two elements having the same tangents: above with a uniform markers distribution and below, with a non-uniform marker distribution. (For interpretation of the references to color in this figure, the reader is referred to the web version of this article.)

where $\boldsymbol{t}_k$ and $\boldsymbol{t}_{k-1}$ are the tangent vectors at markers k and $k-1$ (red circles in Fig. 4) that define the front element e (see red line in Fig. 4(*a*)). This approach is also used in [11,12,26,8,9,27–29]. A new method for the calculation of the tangent $\boldsymbol{t}_k$ at the marker position is proposed in section 3.1.

Note that there is another approach that consists in calculating this force at marker position [see [30,7,31,32,25,33]]. Considering the difference between the tangents $\boldsymbol{t}_e$ and $\boldsymbol{t}_{e+1}$ of the neighbor front elements e and $e+1$ as shown in Fig. 4(*b*), the force $\boldsymbol{f}_k$ at the marker k is calculated as:

$$\boldsymbol{f}_k = \sigma\,(\boldsymbol{t}_{e+1} - \boldsymbol{t}_e) \tag{16}$$

Although both formulations ensure that the total force on any closed surface is equally zero, there is a crucial difference between the two methods. We consider the two interfaces (ABC) and $(A'B'C')$ described by two elements in Fig. 4(c). The elements AB and $A'B'$ (resp BC and $B'C'$) have the same unit tangents but the curvature and so the capillary contributions at point B and B' are different. However, if the tangent $\boldsymbol{f}_B$ at marker B is calculated using equation (16), then $\boldsymbol{t}_{BC} - \boldsymbol{t}_{AB} = \boldsymbol{t}_{B'C'} - \boldsymbol{t}_{A'B'}$ and both interfaces (ABC) and $(A'B'C')$ will contribute at marker B with an identical capillary force $\boldsymbol{f}_B = \boldsymbol{f}_{B'}$ while they clearly have different curvatures. The consequence of this problem were noticed but not solved in [7].

We now consider the discretization of the Dirac distribution function. For example at an $i+1/2$ cell face, $D_{i+1/2,j}(\boldsymbol{x}_e)$ is approximated by [34]

$$D_{i+1/2,j}(\boldsymbol{x}_e) = \frac{1}{\Delta x \Delta y}\delta\left(\frac{x_{i+1/2,j} - x_e}{\Delta x}\right)\delta\left(\frac{y_{i+1/2,j} - y_e}{\Delta y}\right) \tag{17}$$

where

$$\delta(r) = \begin{cases} \delta^*(r) & \text{if } |r| \le 1, \\ 1/2 - \delta^*(2-|r|) & \text{if } 1 < |r| < 2, \\ 0 & \text{if } |r| \ge 2 \end{cases} \tag{18}$$

and

$$\delta^*(r) = \frac{3 - 2|r| + \sqrt{1 + 4|r| - 4r^2}}{8} \tag{19}$$

Cell center quantities are linearly interpolated from the faces. In a uniform staggered grid, this is achieved by:

$$F'_{xi,j} = \frac{1}{2}(F'_{xi+1/2,j} + F'_{xi-1/2,j}),\ F'_{yi,j} = \frac{1}{2}(F'_{yi,j+1/2} + F'_{yi,j-1/2}) \tag{20}$$

$$G_{xi,j} = \frac{1}{2}(G_{xi+1/2,j} + G_{xi-1/2,j}),\ G_{yi,j} = \frac{1}{2}(G_{yi,j+1/2} + G_{yi,j-1/2}) \tag{21}$$

The curvature at cell centers is then calculated by:

$$\kappa_{i,j} = \begin{cases} \frac{F'_{xi,j}G_{xi,j} + F'_{yi,j}G_{yi,j}}{\sigma(G^2_{xi,j} + G^2_{yi,j})} & \text{if } G^2_{xi,j} + G^2_{yi,j} > 0, \\ 0 & \text{if } G^2_{xi,j} + G^2_{yi,j} = 0 \end{cases} \tag{22}$$

The following filter function is introduced:

$$c_{i,j} = \begin{cases} 1 & \text{if } G^2_{xi,j} + G^2_{yi,j} \neq 0, \\ 0 & \text{if } G^2_{xi,j} + G^2_{yi,j} = 0 \end{cases} \tag{23}$$

and the curvatures at the face center are recovered with:

$$\kappa_{i+1/2,j} = \begin{cases} \frac{\kappa_{i,j}c_{i,j} + \kappa_{i+1,j}c_{i+1,j}}{c_{i,j}+c_{i+1,j}} & \text{if } c_{i,j} + c_{i+1,j} \neq 0, \\ 0 & \text{if } c_{i,j} + c_{i+1,j} = 0 \end{cases} \tag{24}$$

$$\kappa_{i,j+1/2} = \begin{cases} \frac{\kappa_{i,j}c_{i,j} + \kappa_{i,j+1}c_{i,j+1}}{c_{i,j}+c_{i,j+1}} & \text{if } c_{i,j} + c_{i,j+1} \neq 0, \\ 0 & \text{if } c_{i,j} + c_{i,j+1} = 0 \end{cases} \tag{25}$$

2.4. Advection of markers

Once mass and momentum equations (1)–(2) are solved and a conservative velocity field is obtained, markers are advected integrating in time:

$$\frac{d\boldsymbol{x}_k}{dt} = \boldsymbol{U_k} \tag{26}$$

using an explicit first order (FO) scheme:

$$\boldsymbol{x}_k^{n+1} = \boldsymbol{x}_k^n + \boldsymbol{U}_k \Delta t \tag{27}$$

where n stands for the current time step. The marker velocity $\boldsymbol{U}_k$ is interpolated from the Eulerian grid through:

$$\boldsymbol{U}_k = \sum_{ij} \Delta x \Delta y \boldsymbol{U}_{ij} D_{ij}(\boldsymbol{x}_k) \tag{28}$$

For comparison purposes, the marker advection will also be solved inside the momentum three-step Runge–Kutta cycle and eq. (26) will be calculated using the three order ($RK3$) scheme:

$$\frac{\boldsymbol{x}_k^{m,n} - \boldsymbol{x}_k^{m-1,n}}{\Delta t} = (\alpha_m + \beta_m)\boldsymbol{U}_k^{m-1,n} \tag{29}$$

where α_m and β_m are the Runge–Kutta coefficients of the Navier–Stokes solver:

$$\alpha_1 = \beta_1 = 4/15;\ \alpha_2 = \beta_2 = 1/15;\ \alpha_3 = \beta_3 = 1/6 \tag{30}$$

The subscript m is the current $RK3$ step and $\boldsymbol{U}_k^m$ is the corresponding intermediate velocity. The $RK3$ is initialized with the position and velocity at time n: $\boldsymbol{x}_k^{0,n} = \boldsymbol{x}_k^n$ and $\boldsymbol{U}_k^{0,n} = \boldsymbol{U}_k^n$. The new position at time $n+1$ is $\boldsymbol{x}_k^{n+1} = \boldsymbol{x}_k^{3,n}$. By default, in all the simulations reported in this work, the markers advection will be performed using the first order Euler scheme FO except when the Runge–Kutta $RK3$ is explicitly mentioned.

3. Improvement to the marker method

3.1. New tangent calculation at markers position

The calculation of tangents at the markers position has been addressed in the literature by fitting/interpolating functions on the markers position and then calculating the tangents analytically [see for example [8,9]]. In this work we consider that two neighbor front elements e and $e+1$ share a common curvature center, as depicted in Fig. 5.

By simple geometrical considerations, the tangent $\boldsymbol{t}_k$ at marker k can be calculated from the tangents $\boldsymbol{t}_e$ and $\boldsymbol{t}_{e+1}$ of the elements e and $e+1$ considering that markers $k-1$, k and $k+1$ are located on the same circle:

$$\boldsymbol{t}_k = \frac{\Delta s_{e+1}\boldsymbol{t}_e + \Delta s_e \boldsymbol{t}_{e+1}}{\sqrt{\Delta s_{e+1}^2 + \Delta s_e^2 + 2\Delta s_{e+1}\Delta s_e \boldsymbol{t}_e \cdot \boldsymbol{t}_{e+1}}} \tag{31}$$

As detailed in Appendix B, relation (31) is an exact geometrical relation so no additional error from interpolation is introduced here.

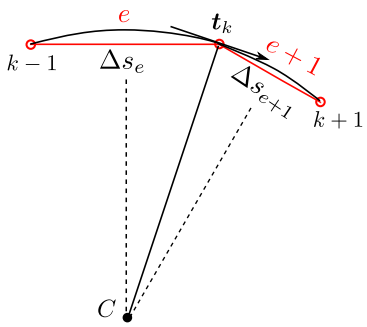

Fig. 5. Schematics of a front. In red, the discrete front defined by elements e and $e+1$. Their tangent $\boldsymbol{t}_e$ and $\boldsymbol{t}_{e+1}$ (not shown) are used in the calculation of the tangent $\boldsymbol{t}_k$ at marker k. In black the circle of center C defined by markers $k-1$, k and $k+1$. (For interpretation of the references to color in this figure, the reader is referred to the web version of this article.)

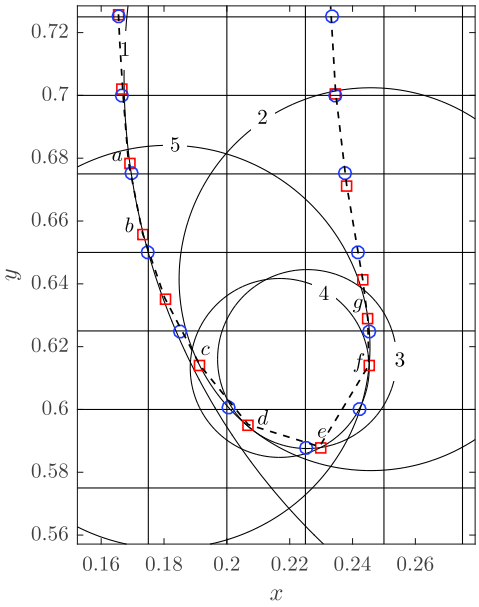

Fig. 6. Description of the reconstruction procedure. The interface shape is a part of the shape of a rising bubble with $\rho_1/\rho_2 = 1000$, $\mu_1/\mu_2 = 100$, $\sigma = 1.96$, $g = 0.98$, $Re = 35$, $Eo = 125$ [17] (see section 6). Circles 1, 2, 3, 4 and 5 are generated with the curvature of the front elements ab, cd, de, ef and fg respectively. □ Markers before reconstruction; ○ Markers after reconstruction located on the Eulerian grid. (For interpretation of the references to color in this figure, the reader is referred to the web version of this article.)

3.2. The new front reconstruction method

It is well known that markers may drift along the interface due to the fluids motion. In the literature, keeping a reasonable density of markers on the front can be achieved by including and removing front elements given a certain size threshold [see [11,12]]. A more sophisticated and automated procedure can be found in [9], where an interpolating curve is used to obtain an homogeneous distribution. Also, an artificial tangential velocity can be calculated and added to the marker velocity to produce a front with a uniform distribution of markers [see [13,25]]. A more robust procedure is proposed in [7], where an optimum indicator function is introduced to preserve the mass and is used to intersect the Eulerian faces to produce new markers. However, an increase in spurious velocities is then reported because of the non-uniform marker distribution resulting of the reconstruction.

In this work, we propose a new front reconstruction method with the objective to keep the property of the marker method for the reduction of spurious velocities. The method consists in a local reconstruction of the interface using for each element e a circle $\mathcal{C}_e$ of radius R_e determined using the pair of markers $k-1$ and k that define e. The intersection between this circle $\mathcal{C}_e$ and the Eulerian grid will be the base of the reconstruction process. The radius R_e is determined using the Frenet relation for the local curvature $R_e^{-1}\boldsymbol{n} = d\boldsymbol{t}/ds$. The radius R_e is then calculated for the element e using the tangents $\boldsymbol{t}_{k-1}$ and $\boldsymbol{t}_k$ at markers $k-1$ and k as:

$$R_e^{-1} = \left\| \frac{\boldsymbol{t}_k - \boldsymbol{t}_{k-1}}{\Delta s} \right\| \tag{32}$$

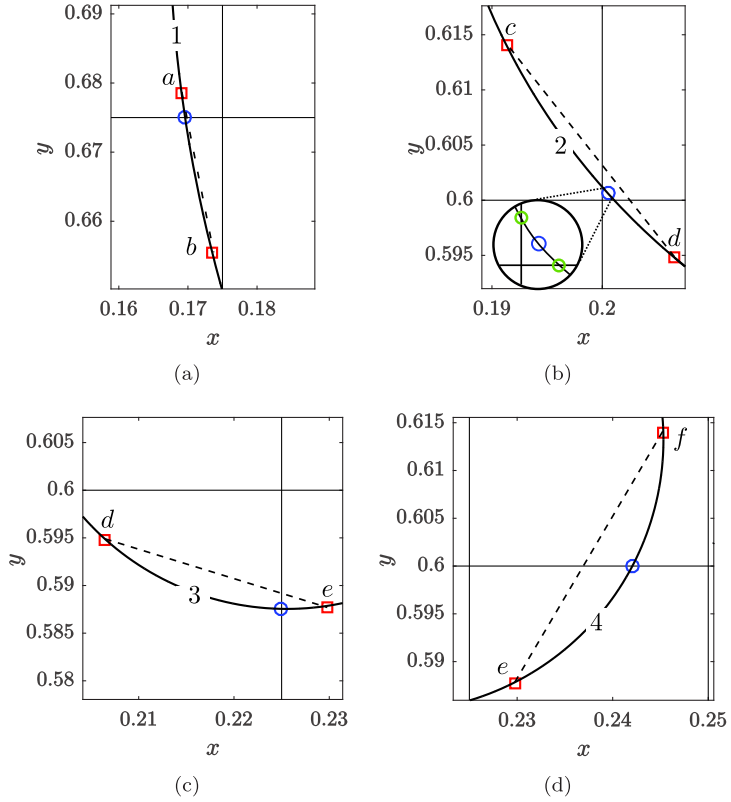

Fig. 7. Zoom from Fig. 6 on front elements (a) ab, (b) cd, (c) de and (d) ef. □ Before reconstruction; ○ After reconstruction. (For interpretation of the references to color in this figure, the reader is referred to the web version of this article.)

The unit tangents $\boldsymbol{t}_{k-1}$ and $\boldsymbol{t}_k$ are calculated using the new expression proposed in this work (relation (31) in section 3.1). The circle center location with respect to the interface is defined considering the sign of the product $\boldsymbol{n}_e \cdot (\boldsymbol{t}_k - \boldsymbol{t}_{k-1})$. Once this circle $\mathcal{C}_e$ is determined, it is intersected with the faces of the Eulerian grid. In practice the intersection is only made with the Eulerian cells in the vicinity of the element. Then new markers are defined as the intersecting point located inside the circular arc limited by the two considered markers $k-1$ and k of element e. Since front elements do not overlap (coalescence process are not addressed in this work), the intersecting points for each element are unique. Fig. 6 shows a typical reconstruction process. The front before reconstruction is represented by the red squares. For each elements ab, cd, de, ef and fg, the circles 1, 2, 3, 4 and 5 are constructed. The intersections between these circles and the Eulerian grid faces define the new front markers represented using blue circles in the figure.

Fig. 7 shows in detail selected elements and their associated circles used for the reconstruction. The case depicted in Fig. 7(b) deserves a special treatment. Circle 2 intersects the Eulerian grid close to a corner. In such situation, two new markers (in green in Fig. 7(b)) are generated and they form a new front element of short length Δs_e. The closer the circle make the intersection to the corner, the smaller is the resulting front element (in an extreme case $\Delta s_e = 0$). The effect of having small elements will be discussed in section 5. A threshold value Δs_{min} is introduced to control the minimum size of the elements. If $\Delta s_e \leq \Delta s_{min}$ the markers k and $k-1$ are fused together to avoid small elements. The procedure for this fusion is simple. Following the method described above a circle $\mathcal{C}_e$ is determined based on the two markers to fuse. They are replaced by an unique marker located at the center of the circular arc between the two markers. Fig. 7(b) shows the result of such fusion. It will be shown in the following that the reconstruction is not necessary at each time step. We note n_t the number of iterations between two reconstructions. It is worth mentioning that the radius R_e in equation (32) is only used in the reconstruction process and is not used in the calculation of the capillary force contribution.

4. Validation of the new tangent calculation

It has been reported in [7] that the hybrid formulation for the capillary contribution described in section 2.3 only reduces spurious velocities close to machine precision when a uniform distribution of markers is used. In this section, we first reproduce the test proposed in [7] for a static drop and then we extend the validation to the translating drop test case. We evaluate the new tangent formulation proposed in this work for the calculation of the capillary force (combination of equations (15) and (31)). In particular, we test if spurious velocities can be reduced to machine precision when a non-

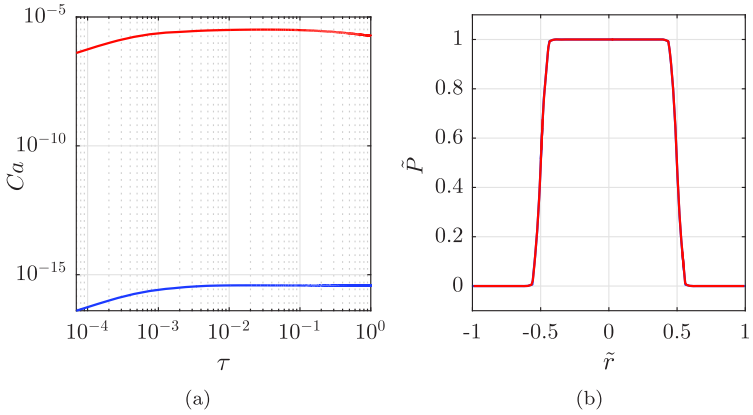

Fig. 8. 2D static drop test case. The capillary force is calculated using the original hybrid formulation of [7] (equation (16)). Comparison between a uniform (——) and a random distribution of markers (——). (a) Maximum normalized velocity evolution. (b) Normalized pressure at $y = 0.5$. (For interpretation of the references to color in this figure, the reader is referred to the web version of this article.)

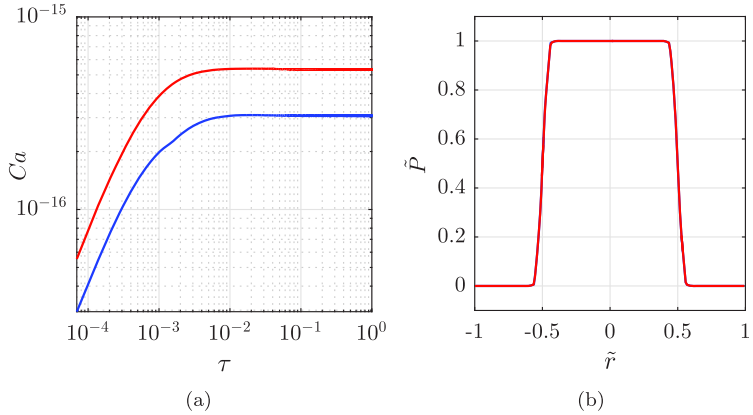

Fig. 9. 2D static drop test case. New calculation of the capillary force (equations (15) and (31)). Comparison of a uniform (——) and a random distribution of markers (——). (a) Maximum normalized velocity evolution. (b) Normalized pressure at $y = 0.5$. (For interpretation of the references to color in this figure, the reader is referred to the web version of this article.)

uniform distribution of markers is considered. For the tests reported in this section, the reconstruction procedure described in section 3.2 is not applied.

4.1. The static drop test case

A 2D drop with radius $R = 0.25$ is initialized in a regular 50×50 grid of size $L \times H = 1 \times 1$. Having all the fluid properties set to 1, the corresponding Laplace number is $La = \rho D\sigma/\mu^2 = 0.5$. For this test, markers are advected using the first order FO time integration scheme (equation (27)). Results are shown in Fig. 8 where two distributions of markers are compared. In blue, the interface is initialized with a uniform distribution of markers such that $\Delta s = \Delta x$. In red, the interface is initialized with a random distribution of markers. The minimum and maximum element sizes are $\Delta s_{min} = 0.3\Delta x$ and $\Delta s_{max} = \Delta x$, respectively. The calculation of the local surface tension force $\boldsymbol{f}$ is first performed using the hybrid method from [7] corresponding to equation (16).

The maximum velocity U_{max} inside the domain is reported in Fig. 8(a) using the capillary number $Ca = \mu U_{max}/\sigma$ as a function of the normalized time $\tau = t/\sqrt{\rho D^3/\sigma}$. When using an uniform distribution of markers, a maximum capillary number close to machine precision is obtained. The use of a non-uniform distribution of markers increases the maximum capillary number Ca up to 8 orders of magnitude. However, the pressure on a line crossing the center of the bubble seems to be unaffected and correctly predicted in both uniform and non-uniform distributions of markers. This is shown in Fig. 8(b), where the radial coordinate and the pressure are respectively normalized as $\tilde{r} = (x - x_c)/x_c$ and $\tilde{P} = P/(\sigma/R)$ where x_c is the position of the bubble center.

The same test is now repeated using the new method proposed here for the calculation of the capillary force (equations (15) and (31)). As can be seen in Fig. 9(a), in both uniform and non-uniform distributions of makers the capillary number is now close to machine precision. Pressure at $y = 0.5$ obviously shows no variation for both distributions (see Fig. 9(b)).

The influence of the Laplace number La on the spurious velocities for the non-uniform distribution of markers is now analyzed. The density ρ and the dynamic viscosity μ of both fluids are set to 1, while the surface tension is varied to

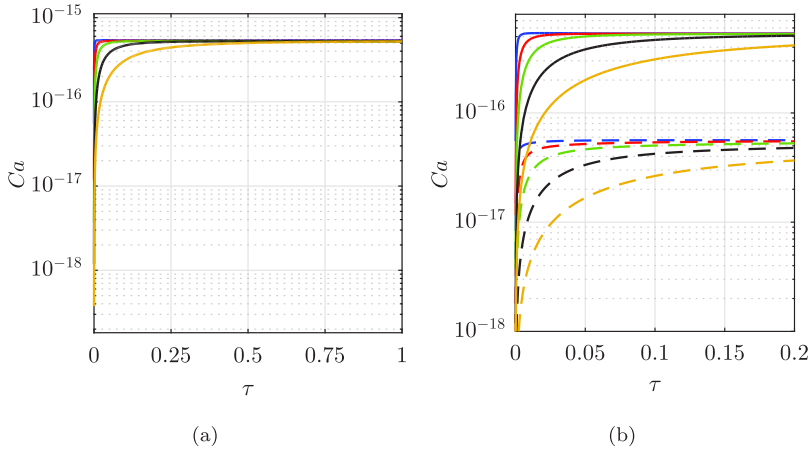

Fig. 10. Effect of La on the spurious current convergence for a non-uniform distribution of markers. (a) Maximum velocity: ——, $La = 0.5$; ——, $La = 12$; ——, $La = 120$; ——, $La = 1200$; ——, $La = 12000$. (b) Maximum and RMS velocities: - - -, $La = 0.5$; - - -, $La = 12$; - - -, $La = 120$; - - -, $La = 1200$; - - - $La = 12000$. (For interpretation of the references to color in this figure, the reader is referred to the web version of this article.)

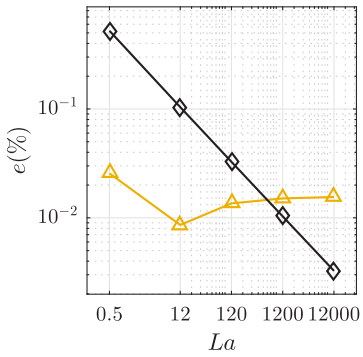

Fig. 11. Static drop test case. Laplace number effect on the pressure jump. Relative error for ◇—, ΔP_{max}; △—, ΔP_{avg}.

consider the Laplace numbers $La = 0.5, 12, 120, 1200$ and 12000. The corresponding results are shown in Fig. 10(a) where the evolution of the normalized maximum velocity is reported using the capillary number Ca. The Laplace number affects the initial evolution of the velocity, but in all cases a stabilization is always achieved with similar values close to machine precision. In Fig. 10(b) the RMS dimensionless velocity is shown up to $\tau = 0.2$. The rate of convergence in time for the RMS velocity is quite similar to that of the maximum velocity, its value being one order of magnitude smaller. Note that results close to machine precision where also found with a VOF-CSF method [35] and with the Level Set Sharp Surface Force method [20] but a longer time for convergence was observed for these methods.

We define the average pressure jump ΔP_{avg} and the maximum pressure jump ΔP_{max}, both normalized by the Laplace pressure σ/R. The former is found by taking the difference of the area weighted average of the pressure inside $(0.5 < C \leq 1)$ and outside $(0 \leq C < 0.5)$ the drop, while the latter is calculated by the difference between the maximum and the minimum pressure inside the domain. The relative error for ΔP_{max} and ΔP_{avg} are defined as $|1 - \Delta P_{max}\, R/\sigma|$ and $\left|1 - \Delta P_{avg}\, R/\sigma\right|$, respectively. They are reported as function of the Laplace number in Fig. 11. The error in ΔP_{max} has a tendency to decrease with La, while ΔP_{avg} it is close to 0.01% for any La. A grid test dependence is reported in Fig. 12. The values of both the Maximum and RMS velocities remains close to machine precision for all the grid considered. However, we observe the growth of the maximum and RMS velocities with grid resolution (Fig. 12(a)). The same trend is found for the maximum pressure jump error (Fig. 12(b)) while the error in the average pressure shows a decrease with grid resolution. The reason of the observed lack of convergence might be due to round-off errors that can be important at this level of precision. Taking equation (17) as an example, it is clear that when $\Delta x = \Delta y = \Delta \to 0$ then $D_{i,j} \to \infty$. Analytically, this does not affect $\kappa_{i,j}$ in equation (22), since the denominator in Δ^2 of $D_{i,j}$ vanishes through $\boldsymbol{F}'_\sigma$ and $\boldsymbol{G}$. However, the successive operations with Δ^2 might bring round-off errors as $\Delta \to 0$. To avoid the error, the surface tension force contribution should be rewritten using $D_{i,j}$ defined as $D_{i,j} = \delta(x_{i,j} - x'_k)\delta(y_{i,j} - y'_k)$ but this simplification only works in uniform Eulerian grids. The analysis and correction of round-off errors (if possible) must be extended to all routines in the solver, a task that was outside of the scope of this work.

Next we evaluate the effect of the time step Δt on the reduction of spurious velocities and the FO and $RK3$ schemes for the marker advection are compared. The case of $La = 12000$ is chosen for this test and results are reported in Fig. 13

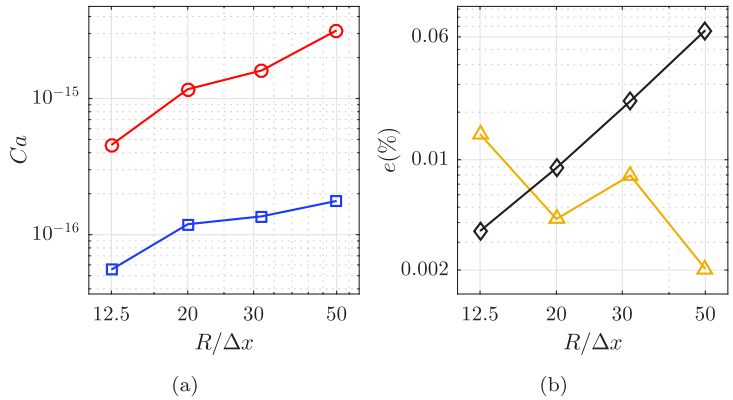

Fig. 12. Static drop test case. Effect of $R/\Delta x$ ($\Delta\tau = 0.15$). (a), Maximum Velocity; , RMS Velocity. (b) Relative error for , ΔP_{max}; , ΔP_{avg}.

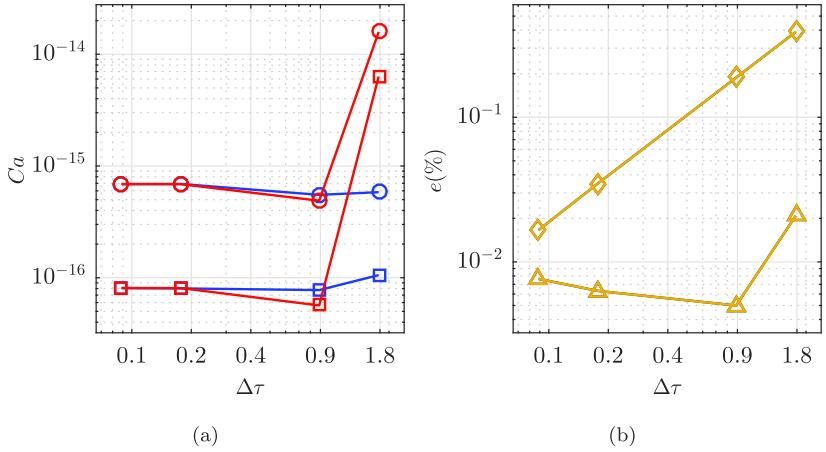

Fig. 13. Static drop test case. Effect of Δt ($R/\Delta x = 12.5$). (a) , Maximum Velocity (FO); , RMS Velocity (FO); , Maximum Velocity ($RK3$); , RMS Velocity ($RK3$). (b) Error for , ΔP_{max} (FO); , ΔP_{avg} (FO); , ΔP_{max} ($RK3$); , ΔP_{avg} ($RK3$). (For interpretation of the references to color in this figure, the reader is referred to the web version of this article.)

where the time step has been normalized using the characteristic time as $\Delta\tau = \Delta t/\Delta t_\sigma$ where Δt_σ is defined in eq. (5). For all $\Delta\tau$ tested, both maximum and RMS velocities decrease with $\Delta\tau$ and stabilize to a value close to machine precision. FO and $RK3$ schemes give similar spurious velocities except for the larger time step considered ($\Delta\tau \approx 1.8$) where the difference is about 2 orders of magnitude. This is expected given that $RK3$ is a high order scheme of advection so the difference between the two schemes will be noticeable when increasing the time step. There is no noticeable difference between FO and $RK3$ for the relative errors of the pressure jump ΔP_{max} and ΔP_{avg} (Fig. 13(b)). The relative error for the maximum pressure jump ΔP_{max} shows a clear convergence with the reduction of the time step whereas the error in the average pressure is almost constant ($\approx 0.01\%$).

4.2. The translating drop test case

The translating drop test case is a more difficult configuration for the control of spurious velocities [35,24,20]. Indeed, the combined effect of the curvature calculation and the interface advection controls the development of spurious currents [20]. We consider a translating drop of radius $R = 0.2$ inside a unit square domain initialized with a uniform velocity field U_0 (Fig. 14). On the horizontal boundaries the symmetry condition is imposed, while on the vertical boundaries a periodic condition is prescribed. The fluids properties are varied to test different Laplace La and Capillary Ca numbers, keeping the same density and viscosity inside and outside the drop. Markers are initially randomly distributed on the drop surface with element sizes ranging between $\Delta s_{min} = 0.3\Delta x$ and $\Delta s_{max} = \Delta x$. The timescale $t_U = D/U_0$ is used to define the normalized time as $\tau = t/t_U$.

In the reference frame of the translating drop, the velocity should remains zero. So, we define the normalized velocities $\tilde{U}_{max} = max(|U - U_0|)/U_0$ and $\tilde{U}_{RMS} = |U_{RMS} - U_0|/U_0$ to characterize the development of the spurious currents. The evolution of $\tilde{U}$ with time is shown in Fig. 15. The maximum velocity rapidly stabilizes to values close to machine precision for all the Laplace numbers La considered. The RMS velocity however does not perfectly converge with time, a trend that was

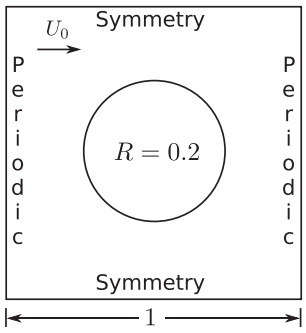

Fig. 14. Domain definition for the translating drop test case.

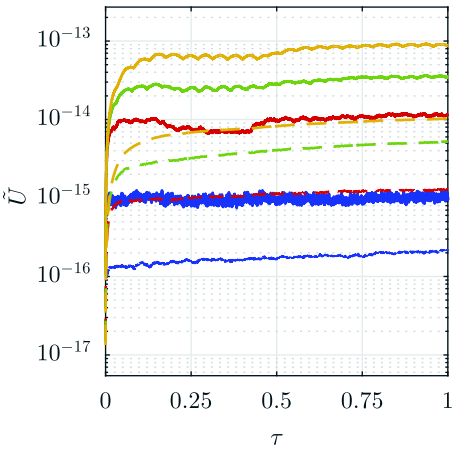

Fig. 15. Translating drop test case. Time evolution of the maximum velocity $\tilde{U}_{max}$ for: ——, $La = 1.2$; ——, $La = 120$; ——, $La = 1200$; ——, $La = 12000$; and for the RMS velocity $\tilde{U}_{RMS}$ for: - - -, $La = 1.2$; - - -, $La = 120$; - - -, $La = 1200$; - - -, $La = 12000$, while keeping $We = 0.4$ and $R/\Delta x = 12.8$. (For interpretation of the references to color in this figure, the reader is referred to the web version of this article.)

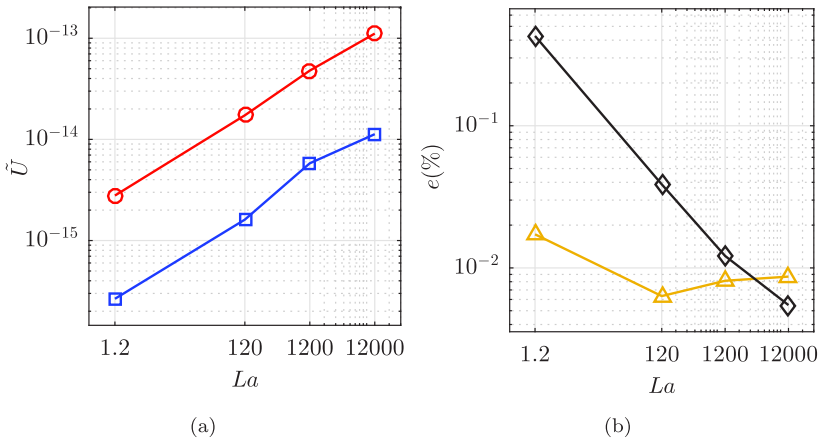

Fig. 16. Translating drop test case. Effect of the Laplace number La. (a) —○—, Maximum Velocity $\tilde{U}_{max}$; —□—, RMS Velocity $\tilde{U}_{RMS}$. (b) Relative error for —◇—, ΔP_{max}; —△—, ΔP_{avg}, while keeping $We = 0.4$ and $R/\Delta x = 12.8$.

noticed in [35] where it is stated that advection induces perturbation on the shape of the interface (hence the curvature calculation). Fig. 16(a) shows the effect of the Laplace number on the maximum and the RMS velocity keeping a constant Weber number $We = \rho U_0^2 D/\sigma = 0.4$. The maximum and RMS velocities both increase with the Laplace number, their maximum values being $\tilde{U} \approx 1 \times 10^{-13}$ and $\tilde{U}_{RMS} \approx 1 \times 10^{-14}$, close to machine precision. The relative error for the maximum pressure jump decreases with La, while the average pressure jump is almost constant (Fig. 16(b)).

The effect of the grid refinement is shown in Fig. 17 for $We = 0.4$ and $La = 12000$. The simulations are conducted with the time step $\Delta\tau = 0.15$ imposed by the stability criteria (5) for the finest grid ($R/\Delta x = 50$). Fig. 17 reports for both the

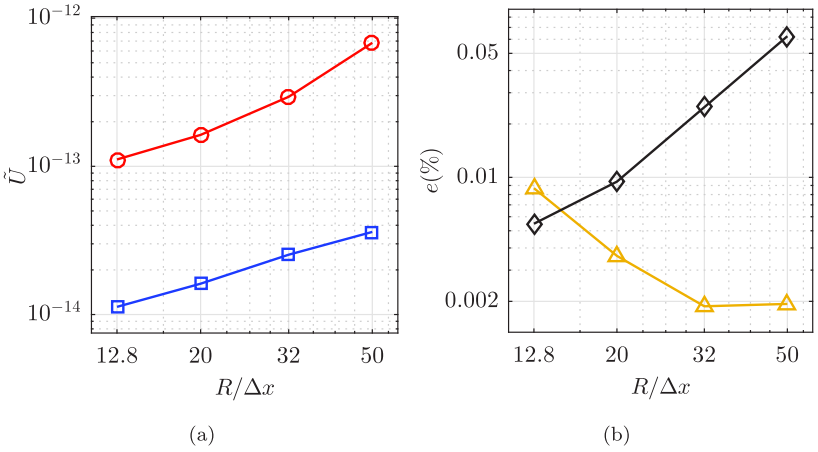

Fig. 17. Translating drop test case for $We = 0.4$ and $La = 12000$. Effect of $R/\Delta x$ ($\Delta\tau = 0.15$). (a) —o—, Maximum $\tilde{U}$; —□—, RMS $\tilde{U}$. (b) Percent error for —◇—, ΔP_{max}; —△—, ΔP_{avg}.

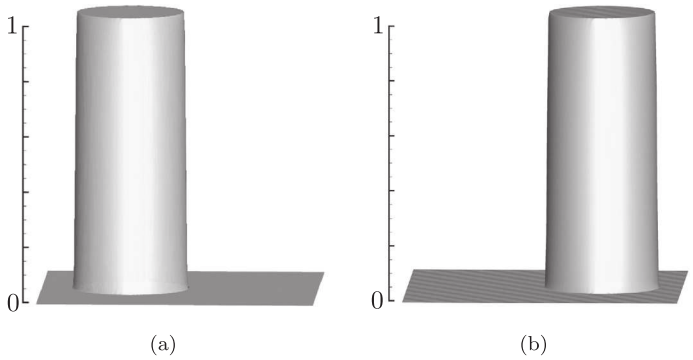

Fig. 18. Translating drop test case. Normalized pressure profile for $R/\Delta x = 50$, $La = 12000$ and $We = 0.4$ at: (a) $\tau = 0.0804$; (b) $\tau = 1.6089$.

velocity and the pressure the same behavior as observed for the static drop test case. The spurious velocity magnitude and the error of the maximum pressure do not decrease with the grid refinement as discussed in section 4.1. However both maximum and RMS velocities remain close to machine precision with values less than 7×10^{-13} and 4×10^{-14}, respectively. Note that this level of spurious velocity is significantly lower than those reported in [35] and [20]. The pressure profile is always sharp and no perturbation could be detected as shown in Fig. 18.

We consider the effect of the time step Δt in Fig. 19(a) for $La = 12000$, $We = 0.4$ and $R/\Delta x = 12.8$. Here the FO and $RK3$ schemes for the marker advection provide different level of spurious velocities. For the error in the pressure the behavior is similar to the one observed for the steady drop test case. The difference for the velocity is more significant. The magnitude of the spurious velocities remains to a very low level but no clear convergence is shown with $\Delta\tau$. In fact, the maximum of spurious velocity is observed for the smallest $\Delta\tau \approx 0.01$ for both the maximum and RMS spurious velocities. This may be explained with the complex coupling between surface tension force calculation and interface advection as outlined in [20]. When we reduce the time step Δt more time steps are required to achieve the same time increasing the number of operations and the amplification of the perturbations. For the same reason, there is no advantage of using the $RK3$ scheme when markers are transported with a uniform velocity.

We end the translating drop test case by considering the effect of the flow capillary number. In practice, numerical simulations are affected by the development of spurious velocities when the characteristic capillary number of the flow is not large enough compared to the characteristic capillary number of the spurious currents. For the drop test case, we define the drop Capillary number as $Ca = \mu U_0/\sigma$ and the spurious velocity capillary numbers as $\widetilde{Ca}_{max} = max(|U - U_0|)\mu/\sigma$ and $\widetilde{Ca}_{RMS} = |U_{RMS} - U_0|\,\mu/\sigma$ for the maximum and RMS spurious velocities, respectively. To provide a complete view of the method performance, we modify the fluid properties to cover a large range of the drop Capillary number such that $10^{-10} \leq Ca \leq 1$. Results are shown in Figs. 20 for both the spurious velocity and the error in the pressure jump. Both $\widetilde{Ca}_{max}$ and $\widetilde{Ca}_{RMS}$ are linearly increasing with Ca but their magnitude remains always about 10 orders of magnitude lower than Ca. For $Ca = O(1)$ we observe that the error in the maximum pressure jump is significantly increased while the error in the average pressure jump is less affected. Fig. 21(a) reports the grid test conducted for $Ca = 10^{-10}$, the smaller capillary number considered here. The time step $\Delta\tau = 0.15$ is imposed by the stability criteria (5) for the finest grid. The evolution

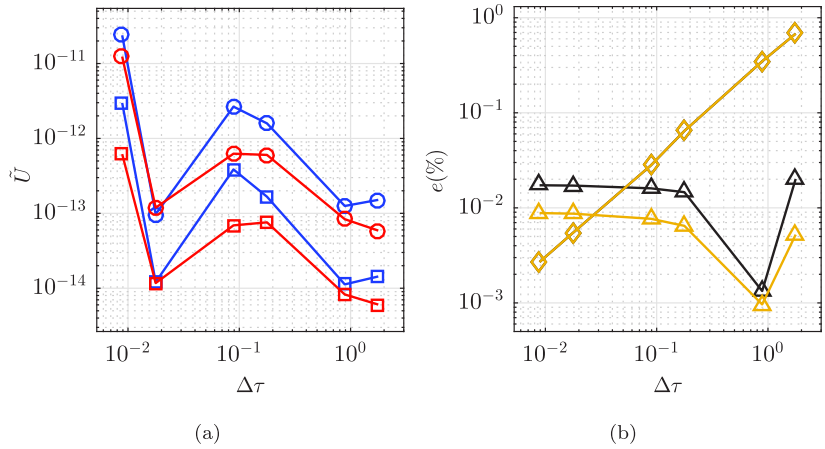

Fig. 19. Translating drop test case. Effect of the time step Δt for $La = 12000$, $We = 0.4$ and $R/\Delta x = 12.8$. (a) —o—, Maximum Velocity (FO); —□—, RMS Velocity (FO); —o—, Maximum Velocity $(RK3)$; —□—, RMS Velocity $(RK3)$. (b) Error for —◇—, ΔP_{max} (FO); —△—, ΔP_{avg} (FO); —◇—, ΔP_{max} $(RK3)$; —△—, ΔP_{avg} $(RK3)$. (For interpretation of the references to color in this figure, the reader is referred to the web version of this article.)

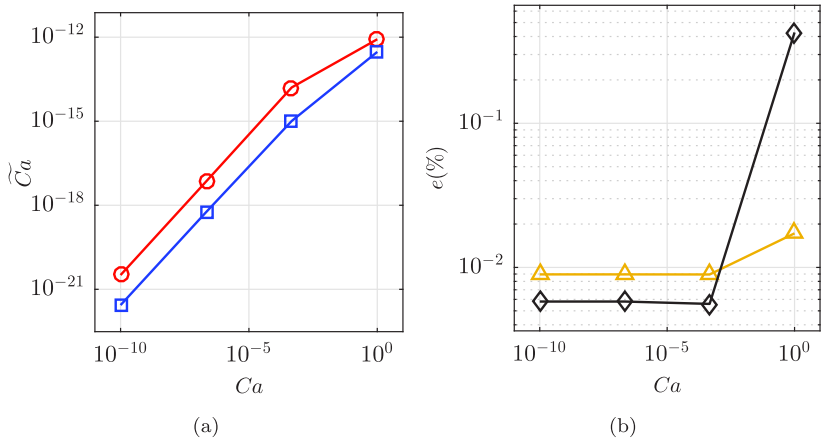

Fig. 20. Translating drop test case with $R/\Delta x = 12.8$. Effect of the drop capillary number Ca. (a) —o—, Maximum spurious velocity; —□—, RMS spurious velocity. (b) Relative error for —◇—, ΔP_{max}; —△—, ΔP_{avg}.

for both the spurious velocity magnitude and the error in the pressure are very similar to those reported in Fig. 17. In particular the magnitude of the spurious velocities increases with the grid refinement but it remains at a very small level. We can conclude that the performance of the method is not sensible of the flow capillary number.

5. Assessment of the reconstruction procedure

We have demonstrated so far that our new method for the capillary calculation with a non-uniform distribution of markers can maintain spurious velocities close to those obtained with a uniform distribution. The objective of this section is now to evaluate the new reconstruction process described in section 3.2. First we check the ability of the reconstruction method to reproduce a given shape. Then the reconstruction procedure is used for the simulation of both the static and translating drop test cases.

5.1. Accuracy of the reconstruction method

To test the accuracy of the reconstruction process, we consider an ellipsoidal interface of equation $x^2/9 + y^2/4 = 1$ in a 12×12 box [see [36] for details on the initialization]. The ellipse front is initialized with markers uniformly distributed. Then the markers are redistributed on the grid cells following the reconstruction procedure. We measure the maximum relative error between the markers y-coordinates obtained after reconstruction and the exact ellipse equation. We vary the ratio $\Delta s/\Delta x$ where Δs is the average length of the elements and Δ_x is the Eulerian grid size. In Fig. 22(a) the number of elements N is varied from 10 to 100 for a fixed grid (16×16 cells) while in Fig. 22(b), the grid size Δx is varied from

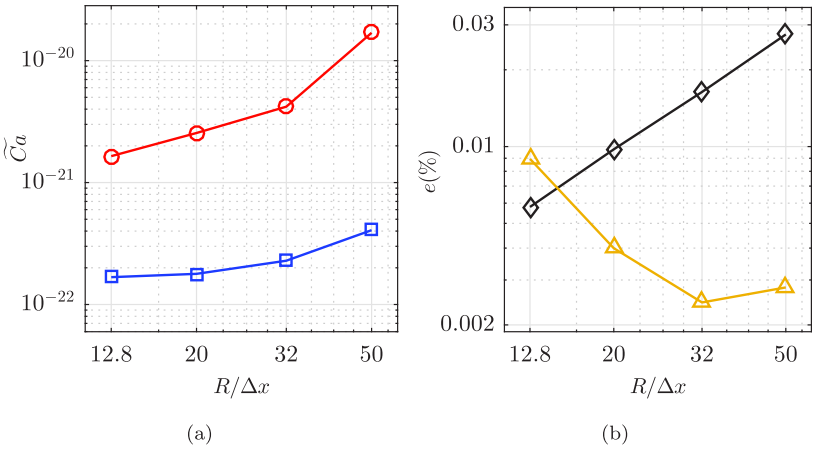

Fig. 21. Translating drop test case. Effect of the grid spacing $R/\Delta x$ for $Ca = 10^{-10}$. (a) —○—, Maximum spurious velocity; —□—, RMS spurious velocity. (b) Relative error for —◇—, ΔP_{max}; —△—, ΔP_{avg}.

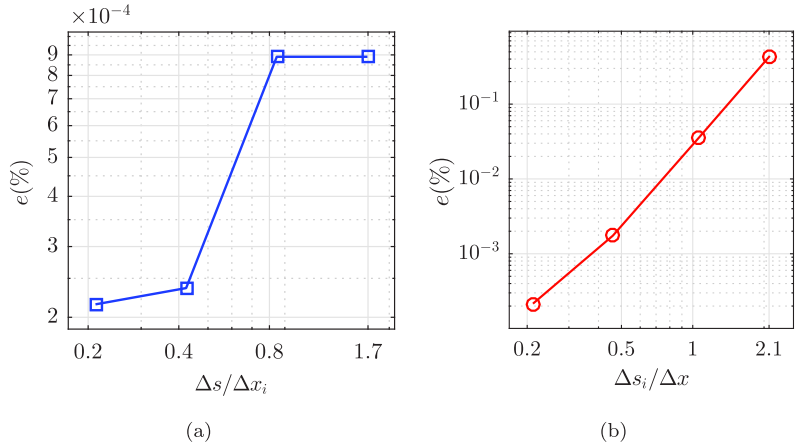

Fig. 22. Effect of $\Delta s/\Delta x$ for the reconstruction of the ellipse $x^2/9 + y^2/4 = 1$: (a) Varying the number of Lagrangian markers Δs_i for the grid 16×16, (b) Varying the Eulerian grid size Δx_i for 100 markers.

16×16 to 168×168 cells for a fixed number of elements ($N = 10$). For clarity we note Δx_i (resp. Δs_i) when the grid size (resp. the element length) is varied.

Fig. 22(a) shows that the error decreases when decreasing $\Delta s_i/\Delta x$ on a given grid. Indeed, the shape description is improved by the initial marker distribution when their number is increased. The maximum error is around 0.4% for the maximum ratio tested ($\Delta s_i/\Delta x = 2.1$). Fig. 22(b) also shows the decrease of the error when decreasing $\Delta s/\Delta x_i$. When the Eulerian grid resolution is improved for a fixed number of markers (increase in $\Delta s/\Delta x_i$), the error on the shape increases. Indeed, when $\Delta s/\Delta x_i$ is increased for a fixed number of elements, the circle $\mathcal{C}_e$ generated from the two markers of each element e intersects an increasing number of cells generating new markers located on the circle $\mathcal{C}_e$ that is a local approximation of the ellipse shape. The error with the ellipsoidal shape of reference is then increased. Thus, front elements of large size can bring errors in the transfer of information between the front and the Eulerian grid. Finally, according to this test, the element length Δs should be chosen smaller than the grid size Δx.

5.2. Optimum value for the threshold Δs_{min}

It has been reported in [7] that the reconstruction process of a non-uniform distribution of markers affects the hybrid formulation capacity to reduce spurious velocities. During the reconstruction process small elements can be generated, typically when the interface position is close to a corner of the Eulerian grid. The question addressed is this section concerns the minimum size Δs_{min} allowed for an element in order to keep the spurious currents close to machine precision. The static drop test case as defined in section 4.1 is first considered. A drop of radius $R = 0.25$ is introduced in a 2D box of size $L \times H = 1 \times 1$ described using a uniform grid spacing $\Delta x = L/25$. The densities and dynamic viscosities are set to one. The surface tension is chosen such that $La = 12000$. The simulation starts with a uniform front with $\Delta s/\Delta x = 1.0$ and the time step $\Delta t = 10^{-5}$ is used. The reconstruction procedure is applied every $n_t = 100$ time steps. The tested values for the

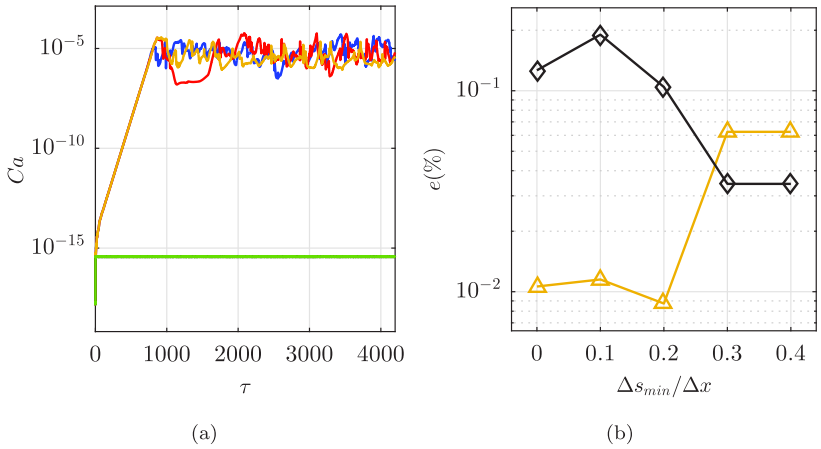

Fig. 23. Static drop test case. Effect of Δs_{min} on the development of the spurious velocities. (a) Maximum Capillary number based on the spurious velocities; $\Delta s_{min} = 0\,\Delta x$; $\Delta s_{min} = 0.1\Delta x$; $\Delta s_{min} = 0.2\Delta x$; $\Delta s_{min} = 0.3\Delta x$; $\Delta s_{min} = 0.4\Delta x$. (b) Relative error for the pressure jump: ΔP_{max}; ΔP_{avg}. (For interpretation of the references to color in this figure, the reader is referred to the web version of this article.)

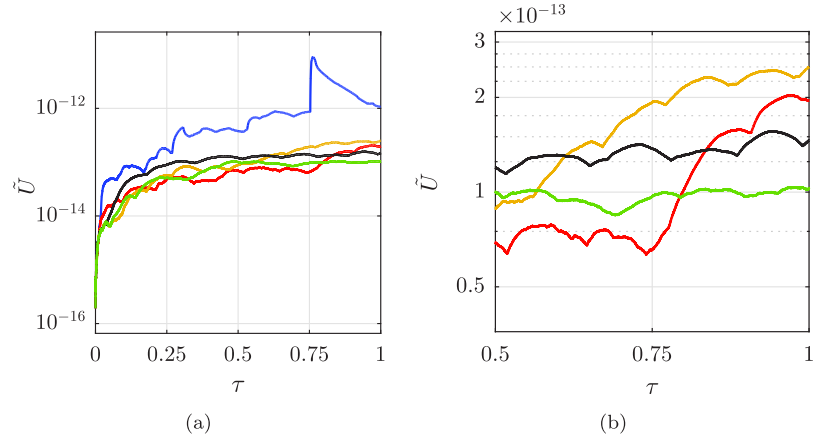

Fig. 24. Translating drop test case. Effect of Δs_{min} on the development of the spurious velocities. (a) Maximum velocity; $\Delta s_{min} = 0.0\Delta x$; $\Delta s_{min} = 0.1\Delta x$; $\Delta s_{min} = 0.2\Delta x$; $\Delta s_{min} = 0.3\Delta x$; $\Delta s_{min} = 0.4\Delta x$. (b) Zoom. (For interpretation of the references to color in this figure, the reader is referred to the web version of this article.)

minimum value Δs_{min} in the reconstruction are $\Delta s_{min} = 0$, 0.1, 0.2, 0.3 and 0.4 times Δx. $\Delta s_{min}/\Delta x = 0$ means that any element of length Δs is conserved. If $\Delta_s \leq \Delta s_{min}$ then the markers are fused together following the procedure explained in section 3.2. The maximum Capillary number based on the spurious velocities is reported in Fig. 23(a). There, two types of evolution are observed. For $\Delta s_{min}/\Delta x = 0$ (blue), $\Delta s_{min}/\Delta x = 0.1$ (red) and $\Delta s_{min}/\Delta x = 0.2$ (orange), the Capillary number stabilizes to a value close to 10^{-5} while for $\Delta s_{min}/\Delta x = 0.3$ (black) and $\Delta s_{min}/\Delta x = 0.4$ (green) the Capillary number remains close to machine precision. It is clear that the condition $\Delta s_{min} > 0.2\Delta x$ is required to obtain spurious velocities comparable to those obtained with a uniform distribution. For $\Delta s_{min} \leq 0.2\Delta x$, the maximum Ca stabilizes to the value observed in Fig. 8(a) (red line) when the force $\boldsymbol{f}$ is calculated at the marker position (equation (16)).

Fig. 23(b) shows the relative error for the maximum and average pressure jumps as a function of $\Delta s_{min}/\Delta x$. The maximum (resp. average) pressure jump error decreases (resp. increases) with $\Delta s_{min}/\Delta x$. For $\Delta s_{min}/\Delta x > 0.2$ both errors meet roughly with a value around 0.05%.

The translating drop test case is now considered with the same domain, grid spacing, time step and fluid properties. The Laplace number is $La = 12000$ and the velocity U_0 is selected to have $We = 0.4$. The front is initialized with a uniform distribution of markers satisfying $\Delta s/\Delta x = 1$. The reconstruction is performed every $n_t = 100$ time steps. Results are shown in Fig. 24. The normalized maximum velocity $\tilde{U}$ seems to converge for all the cases except for the ratio $\Delta s_{min}/\Delta x = 0$ (any element of size Δs being allowed). The zoom in Fig. 24(b) shows that only for the ratios $\Delta s/\Delta x > 0.2$ (black and green lines) the spurious current are stabilized at $\tau = 1$. The error in the pressure jump seems to be independent of Δs_{min} (Fig. 25). The relative error in the average and maximum pressure jumps are around 0.001% and 0.0002%, respectively.

To understand why a small value for Δs_{min} amplifies the spurious velocity, we consider equation (15). Substitution of $\boldsymbol{t}_k$ and $\boldsymbol{t}_{k-1}$ given by equation (31) in the local capillary force contribution $\boldsymbol{f}_e/\sigma = \boldsymbol{t}_k - \boldsymbol{t}_{k-1}$ of the front element e yields:

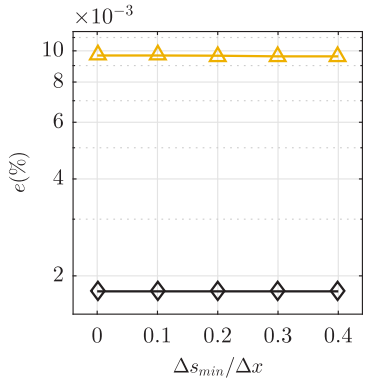

Fig. 25. Translating drop test case: effect of Δs_{min} on the relative error for the pressure jump. ◇ ΔP_{max}; △ ΔP_{avg}.

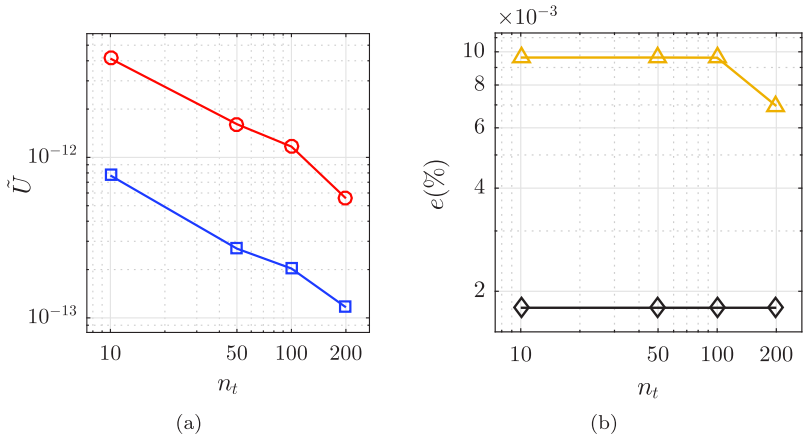

Fig. 26. Translating drop test case. Effect of the number of time step n_t between two reconstructions. (a) ○, Maximum normalized spurious velocity $\tilde{U}$; □, RMS normalized spurious velocity $\tilde{U}$. (b) Relative error for pressure jump; ◇ ΔP_{max}; △ ΔP_{avg}.

$$\boldsymbol{f}_e/\sigma = \frac{\boldsymbol{t}_e\Delta s_{e+1} + \boldsymbol{t}_{e+1}\Delta s_e}{\sqrt{\Delta s_{e+1}^2 + \Delta s_e^2 + 2\Delta s_{e+1}\Delta s_e \boldsymbol{t}_e \cdot \boldsymbol{t}_{e+1}}} - \frac{\boldsymbol{t}_{e-1}\Delta s_e + \boldsymbol{t}_e\Delta s_{e-1}}{\sqrt{\Delta s_e^2 + \Delta s_{e-1}^2 + 2\Delta s_e\Delta s_{e-1}\boldsymbol{t}_{e-1} \cdot \boldsymbol{t}_e}} \tag{33}$$

From relation (33) we see that $f_e/\sigma \to 0$ as $\Delta s_e \to 0$ as expected. However, this relation shows that when $\Delta s_{e-1} \to 0$ (resp. $\Delta s_{e+1} \to 0$) the contribution of the tangent $\boldsymbol{t}_{e-1}$ (resp. $\boldsymbol{t}_{e+1}$) in the calculation of f_e does not vanish. Indeed, considering for example the limit of relation (33) when $\Delta s_{e-1} \to 0$ we get:

$$\boldsymbol{f}_e/\sigma = \frac{\boldsymbol{t}_e\Delta s_{e+1} + \boldsymbol{t}_{e+1}\Delta s_e}{\sqrt{\Delta s_{e+1}^2 + \Delta s_e^2 + 2\Delta s_{e+1}\Delta s_e \boldsymbol{t}_e \cdot \boldsymbol{t}_{e+1}}} - \boldsymbol{t}_{e-1}$$

In fact, when $\Delta s_{e-1}/\Delta s_e \to 0$ (resp. $\Delta s_{e+1}/\Delta s_e \to 0$) maker $k-1$ and $k-2$ (resp. k and $k+1$) becomes very close compared to neighboring markers so that $\boldsymbol{t}_{k-1} \to \boldsymbol{t}_{e-1}$ (resp. $\boldsymbol{t}_k \to \boldsymbol{t}_{e+1}$), giving a non-expected importance of the corresponding elements $e-1$ (resp. $e+1$) in the capillary force contribution of element e. This particular behavior explains why a threshold for Δs is required.

5.3. Frequency of reconstruction

The frequency of reconstruction is now analyzed for the case of the translating drop for $La = 12000$ and $We = 0.4$. Different numbers of time steps $n_t = 10$, 50, 100 and 200 between two reconstructions are compared. Results are shown in Fig. 26. The magnitude of the spurious velocities are kept close to machine precision for all the values of n_t. However, the spurious velocities increase when increasing the frequency of reconstruction. Indeed, errors induced by the circle-segment line intersection are amplified when the frequency of reconstruction is increased. The average error in both the average and mean pressure jump is constant for all the frequency of reconstruction considered.

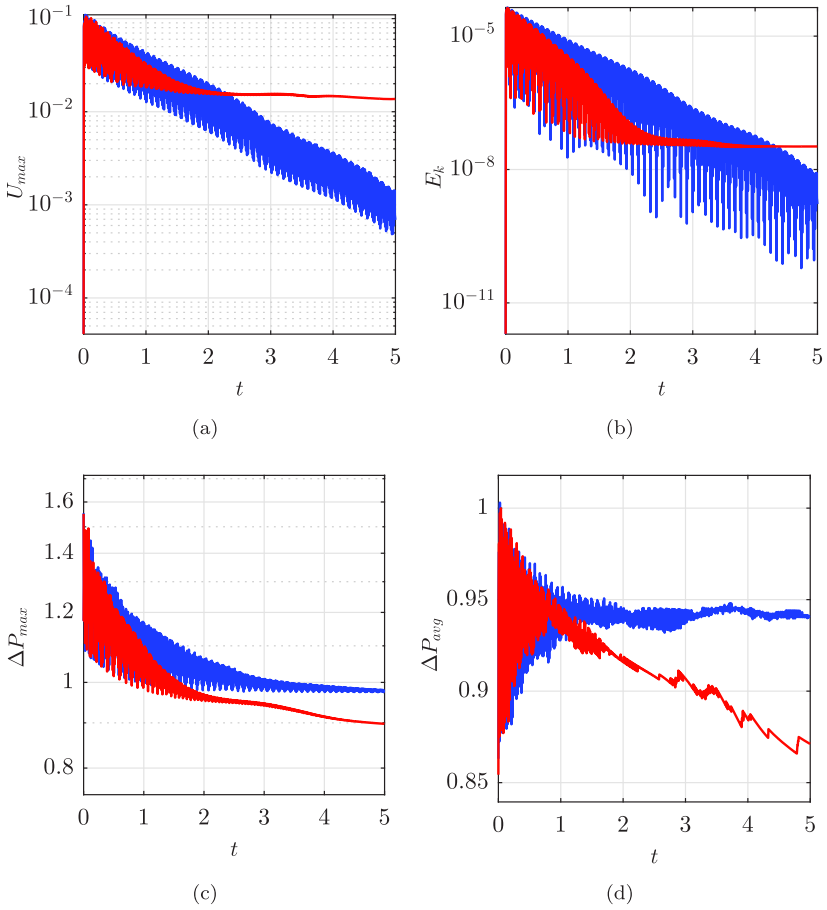

Fig. 27. 2D oscillating drop test case using: —— Front tracking (present); —— Level-Set-CSF. (a) Maximum Velocity evolution. (b) Kinetic Energy evolution. (c) Maximum Pressure jump. (d) Average Pressure jump. (For interpretation of the references to color in this figure, the reader is referred to the web version of this article.)

5.4. 2D oscillating drop test case

We close this series of tests with a test proposed in [36] and reproduced in [7] for a large Laplace number La. An elliptical drop of equation $x^2/0.003^2 + y^2/0.002^2 = 1$ is initialized inside a 0.01×0.01 box with periodic boundary conditions. Properties are set such that the density and viscosity jumps are 1000 and 10 respectively. Surface tension is $\sigma = 0.1$ and the corresponding Laplace number is $La = 5 \times 10^5$. The number of time steps between two reconstructions is $n_t = 1000$ and the grid is made of 64×64 uniform cells. After initialization the drop shape oscillates and converges to a circular shape while the velocity in the domain vanishes.

This test is of particular interest since according to [37], for large density ratios and high Laplace numbers La, intense spurious velocities should be observed and should destroy the interface. We experienced this when we tried for comparison purpose to perform the simulation with the VOF-FCT-CSF (FCT for Flux-Corrected Transport) method of JADIM. The VOF-FCT-CSF method produces catastrophic results not shown here, but we can mention that it took 15000 time steps to destroy the interface. So instead we used the Level Set-CSF method in JADIM for the comparison [see [20] for details on both the VOF-FCT-CSF and the Level Set-CSF methods].

Fig. 27(a) shows the evolution of the maximum velocity inside the domain. It can be seen that the velocity is decreasing with time for the present front-tracking method with reconstruction, while the Level Set-CSF method seems to reach a minimum value at $U_{max} \approx 10^{-2}$. The tendency is confirmed when looking at the kinetic energy evolution ($E_k = \int \rho \boldsymbol{U}^2 dV$). For the Level Set-CSF method the kinetic energy reaches a minimum $E_k \approx 10^{-8}$ while for our front-tracking method E_k is still decreasing at the end of the simulation (see Fig. 27(b)). Figs. 27(c) and 27(d) show the maximum and average pressure jumps normalized using σ/r_{eq} where r_{eq} is the equivalent radius based on the initial ellipse area. The present front-tracking implementation reproduces a correct stabilized pressure jump while it does not converge for the Level-set method. Note that no volume correction [20] was applied here and we found that the drop area starts increasing with time after oscillations have ceased ($t \approx 3$) for the Level-Set-CSF method. At $t \approx 5$, the Level-Set-CSF method shows an increase of 25% of the drop area while the error was found to be less than 1% with the front tracking method.

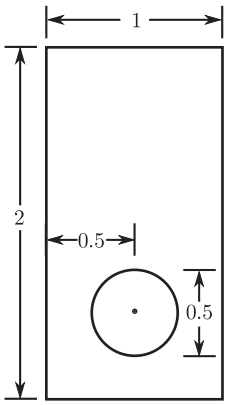

Fig. 28. Initialization of the bubble rising test.

Table 1
Density ratio, viscosity ratio, Reynolds number and Eötvös number for the two selected cases for the simulation of a 2D rising bubble.

Case	ρ_1/ρ_2	μ_1/μ_2	σ	g	Re	Eo
1	10	10	24.5	0.98	35	10
2	1000	100	1.96	0.98	35	125

6. Benchmarking the front tracking method

The new front tracking implementation is now compared to simulations of reference from the literature. We have selected the simulation of 2D rising bubbles [17]. These tests allow us to evaluate relatively large interface deformation to assess the robustness of both the new local surface tension force calculation and the reconstruction method. An initial circular bubble of radius $R = 0.25$ is introduced into a box containing a liquid (see Fig. 28). No slip and symmetry conditions are applied on the horizontal and the vertical boundaries, respectively.

A constant gravity field g is imposed. We introduce the Eötvös number $Eo = 4\rho_1 g R^2/\sigma$ and the Reynolds number $Re = \rho_1 2R^{3/2} g^{1/2}/\mu$ based on the characteristic velocity $\sqrt{gR}$ and the bubble diameter. The fluid properties are reported in Table 1 for the two cases considered.

Four uniform grids are made with $\Delta x = 1/40, 1/80, 1/160$ and $1/320$ and the corresponding time steps $\Delta t = \Delta x/16$ are used. In [17], three different codes have simulated these cases. The code 1 (TU Dortmund, Inst. of Applied Math.) uses a FEM-Level Set method, the code 2 (EPFL Lausanne, Inst. of Analysis and Sci. Comp.) uses a FEM-Level Set method and the code 3 (Univ. Magdeburg, Inst. of Analysis and Num. Math.) uses a FEM-ALE method. For details we refer the reader to [17]. For the two cases considered here, the interface is initialized with a non-uniform distribution of markers. The markers are generated by intersecting the initial bubble shape with the Eulerian grid, with the constraint $\Delta s/\Delta x > 0.2$. The bubble center position Y_c, circularity $\check{c}$ and rise velocity V_c are calculated as follows:

$$Y_c = \frac{\sum_{i,j} C_{ij} y_{ij} A_{ij}}{A_b} \tag{34}$$

$$\check{c} = \frac{2\pi}{L}\sqrt{\frac{A_b}{\pi}} \tag{35}$$

$$V_c = \frac{\sum_{i,j} C_{ij} v_{ij} A_{ij}}{A_b} \tag{36}$$

In these relations, the index ij denote the Eulerian grid cells. A_{ij}, A_b and L are the cell area, the bubble area and the bubble perimeter, respectively. A_b and L are calculated as:

$$A_b = \sum_{ij} C_{ij} A_{ij} \tag{37}$$

$$L = \sum_{k} \Delta s_k \tag{38}$$

Three measures of the relative differences e_i $(i = 1, ..3)$ between the methods are introduced [see [17]]. For any quantity q_t, they are defined as

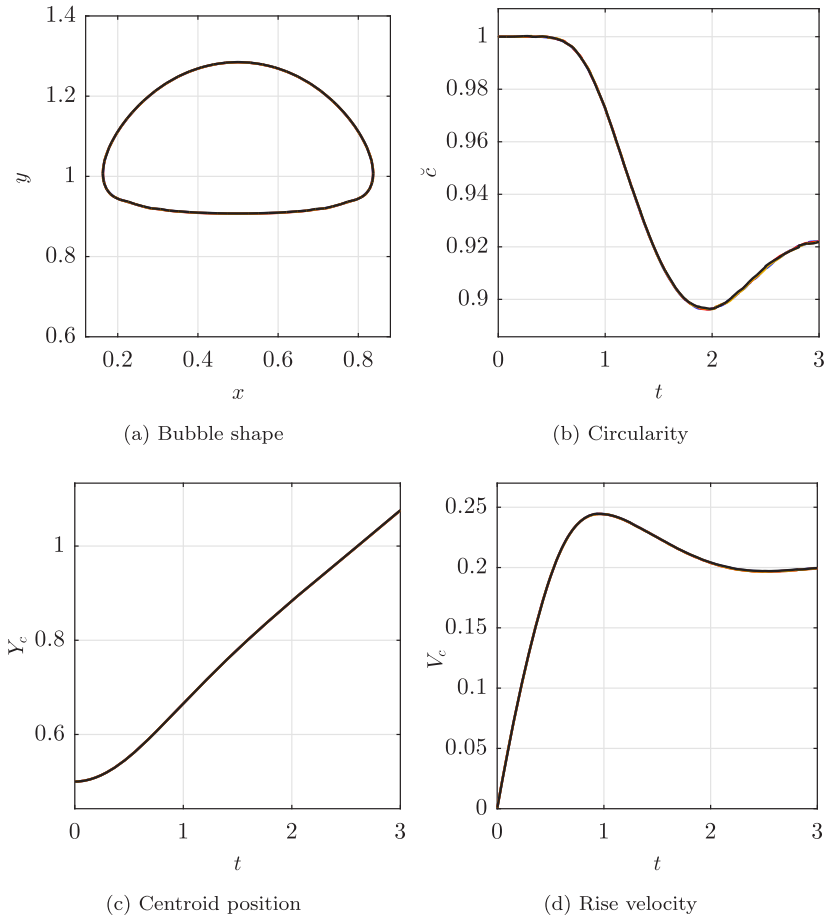

(a) Bubble shape (b) Circularity

(c) Centroid position (d) Rise velocity

Fig. 29. Numerical simulation of a 2D rising bubble in a stagnant fluid (case 1: $Re = 35$ and $Eo = 10$, $\rho_1/\rho_2 = 100$ and $\mu_1/\mu_2 = 10$). (a) Bubble shape, (b) bubble circularity $\check{c}$, (c) bubble center position Y_c and (d) bubble rise velocity V_c. The frequency of the front reconstruction is ——, $n_t = 10$; ——, $n_t = 50$; ——, $n_t = 100$; ——, $n_t = 200$. (For interpretation of the references to color in this figure, the reader is referred to the web version of this article.)

$$e_1 = \frac{\sum_t |q_{t,ref} - q_t|}{\sum_t |q_{t,ref}|} \tag{39}$$

$$e_2 = \left(\frac{\sum_t |q_{t,ref} - q_t|^2}{\sum_t |q_{t,ref}|^2} \right)^{1/2} \tag{40}$$

$$e_3 = \frac{max_t |q_{t,ref} - q_t|}{max_t |q_{t,ref}|} \tag{41}$$

where $q_{t,ref}$ is the quantity of reference. When a grid convergence is performed, the reference quantity $q_{t,ref}$ is the quantity q_t obtained with the finest grid. The values of the different quantities provided by the benchmark are given at http://www.featflow.de/en/benchmarks/cfdbenchmarking/bubble.html.

6.1. Rising Bubble (case 1)

The parameters of case 1 are $Re = 35$, $Eo = 10$, $\rho_1/\rho_2 = 100$ and $\mu_1/\mu_2 = 10$. The frequency of reconstruction is tested with $n_t = 10$, 50, 100 and 200 using the grid size $\Delta x = 1/40$. Results are shown in Fig. 29 and the differences in Table 2. Bubble shape, circularity, centroid position and rise velocity seem to be independent of n_t. Zooms reported in Figs. 30(a) and 30(b) are necessary to see some small differences between the different simulations. Table 2 summarizes for each case the difference with the reference given by code 1. The reported values confirm that the different frequencies of reconstruction considered provide similar results. For the next tests we have chosen $n_t = 100$. Note that the process of front reconstruction could also be triggered by testing at each time step the minimum and maximum front element size and acting accordingly. In this work however, we prescribe a fixed frequency of reconstruction for simplicity.

Table 2
Numerical simulation of a 2D rising bubble in a stagnant fluid (case 1: $Re = 35$ and $Eo = 10$, $\rho_1/\rho_2 = 100$ and $\mu_1/\mu_2 = 10$). Effect of the reconstruction frequency using $\Delta x = 1/40$. The reference for the difference calculation is provided by code 1.

n_t	e_1	e_2	e_3
Circularity $\check{c}$			
10	2.80e−03	3.28e−03	6.07e−03
50	2.76e−03	3.23e−03	6.01e−03
100	2.81e−03	3.28e−03	6.18e−03
200	2.68e−03	3.11e−03	5.84e−03
Centroid position Y_c			
10	2.41e−03	3.37e−03	5.69e−03
50	2.53e−03	3.52e−03	5.96e−03
100	2.46e−03	3.43e−03	5.79e−03
200	2.38e−03	3.28e−03	5.46e−03
Rise velocity V_c			
10	1.30e−02	1.47e−02	2.19e−02
50	1.23e−02	1.40e−02	2.17e−02
100	1.26e−02	1.43e−02	2.15e−02
200	1.34e−02	1.49e−02	2.17e−02

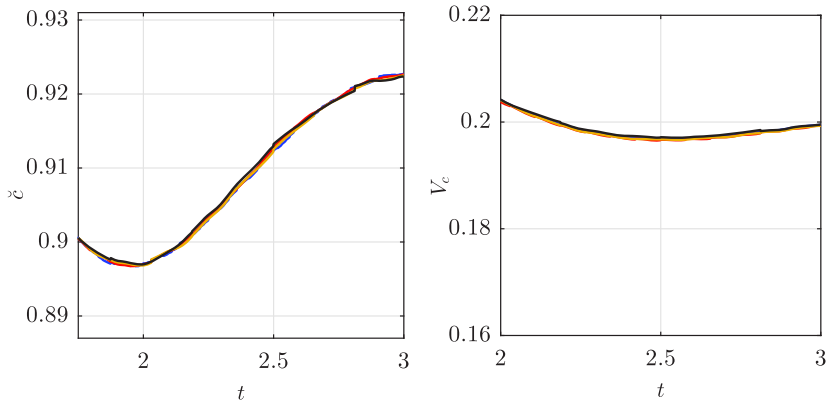

(a) Circularity (b) Rise velocity

Fig. 30. Zoom of (a) Fig. 29(b) and (b) Fig. 29(d). The frequency of the front reconstruction is ——, $n_t = 10$; ——, $n_t = 50$; ——, $n_t = 100$; ——, $n_t = 200$. (For interpretation of the references to color in this figure, the reader is referred to the web version of this article.)

The effect of the grid size is now reported in Fig. 31. The simulations are clearly converging to the case of reference (code 1 with $\Delta x = 1/320$). Interestingly, we can notice that the reported results are few impacted by the grid resolution. The coarsest grid $\Delta x = 1/40$ (in blue) gives very close results to the ones obtained with the finest grid $\Delta x = 1/320$. Circularity seems to be the most affected variable by the coarsest grid. In Fig. 31(b), the maximum difference is observed at $t = 2$, the grid $\Delta x = 1/40$ gives $\check{c} = 0.897$ while the grid of reference $\Delta x = 1/320$ gives $\check{c} = 0.901$, a difference less than 0.5%. According to Fig. 31(a), the difference is mainly located at the maximum of curvature of the bubble. The results obtained with $\Delta x = 1/320$ are now compared in Table 3 with the results obtained with code 1 [17] using the same grid. A very good agreement is found for all the considered quantities. The maximum relative difference is 2.75×10^{-3} for the rising velocity. Additionally, we show in Appendix A a very good agreement between this new front tracking method and both the VOF-FCT-CSF and the Level-Set-CSF methods implemented in our code JADIM [18,24,20]. The mass conservation is also compared and our improved Front tracking method conserves mass at a very good level of 10^{-3}% for this test case.

6.2. Rising Bubble (case 2)

The parameters of case 2 are $Re = 35$, $Eo = 125$, $\rho_1/\rho_2 = 1000$ and $\mu_1/\mu_2 = 100$. The simulation is made using $\Delta x = 1/320$ and the frequency of reconstruction is $n_t = 100$. The comparison of the bubble shape between the different codes is shown in Fig. 32. As observed with code 3 using a FEM-ALE method [17], our front tracking method can not handle break-up automatically, instead, the simulation keep stretching the bubble skirt. However, except in the skirt zone of break-up, the bubble shape is found in very good agreement with the other codes.

The bubble circularity, centroid position and rise velocity are reported in Fig. 33. The circularity evolution for the present front tracking method is nearly identical to that of code 1 up to $t \approx 2.3$. After $t \approx 2.3$, the circularity calculation is affected by the small bubbles generated by the rupture of the bubble skirt (see Fig. 33(a)). The Centroid position shown in Fig. 33(b)

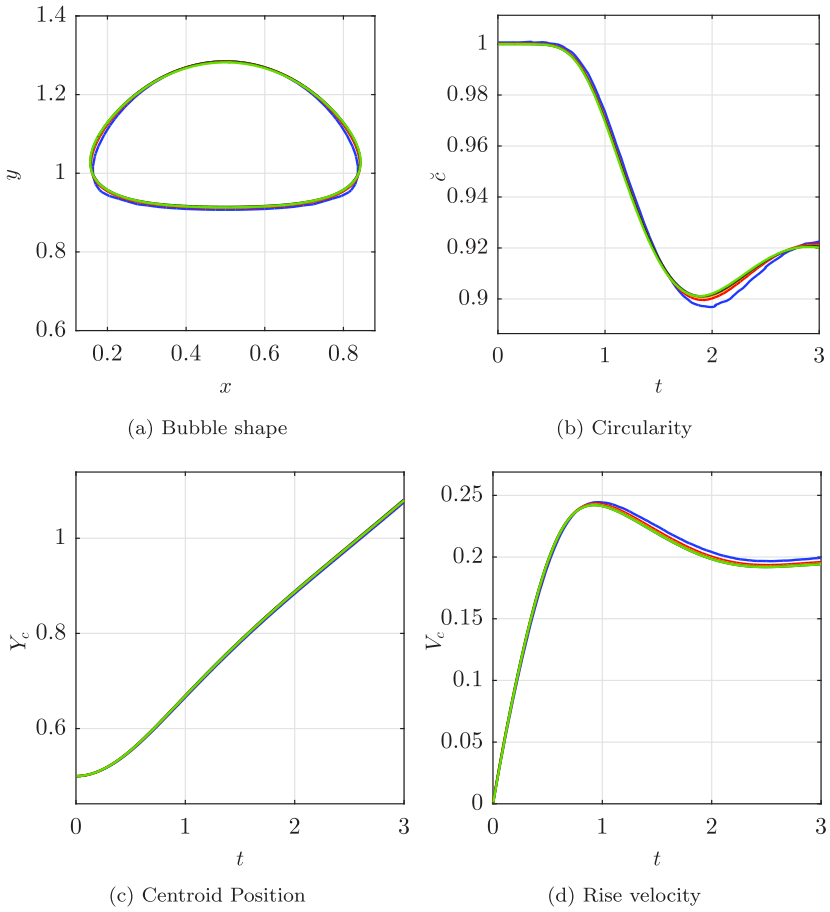

(a) Bubble shape (b) Circularity

(c) Centroid Position (d) Rise velocity

Fig. 31. Evolution of a 2D rising bubble in stagnant fluid (case 1: $Re = 35$ and $Eo = 10$, $\rho_1/\rho_2 = 100$ and $\mu_1/\mu_2 = 10$) for Δx: ——, 1/40; ——, 1/80; ——, 1/160; ——, 1/320; ——, Ref. 1/320. (For interpretation of the references to color in this figure, the reader is referred to the web version of this article.)

Table 3
Comparison between the present front tracking method and code 1 [17] for the 2D rising bubble test case 1 ($Re = 35$, $Eo = 10$, $\rho_1/\rho_2 = 100$ and $\mu_1/\mu_2 = 10$). The grid is $\Delta x = 1/320$.

	e_1	e_2	e_3
Circularity č	9.75e−05	1.22e−04	2.62e−04
Centroid position Y_c	8.69e−05	1.35e−04	2.58e−04
Rise velocity V_c	1.90e−03	2.10e−03	2.75e−03

is virtually independent of the break-up process. The rise velocity is the most sensible quantity for all the codes considered including the present marker method (see Fig. 33(c)) and the maximum difference observed at the end of the simulation is ranging from 6.1% with code 1 to 0.9% with code 2. The difference between our front tracking method and code 1 are reported in Table 4, confirming what Fig. 33 shows: a very good agreement is found and the largest difference is obtained for the circularity.

7. Conclusions

In this work we have improved the 2D front tracking method and we have implemented it inside our in-house code JADIM. The hybrid formulation [7] for the calculation of the surface tension force has been reconsidered with the calculation of tangents at markers position. Spurious currents are then reduced to machine precision for both uniform and non-uniform distribution of markers. The new implementation was tested against the static and translating drop test cases for diverse Laplace and capillary numbers. Tests on the time step Δt and grid spacing Δx reveals that both time and grid convergence can not be observed at this level of precision due to the effect of round-off error.

This new approach to calculate tangents allowed us also to propose a new reconstruction scheme by which the front can be redistributed/reconstructed automatically at prescribed time intervals. This reconstruction scheme is based on circles

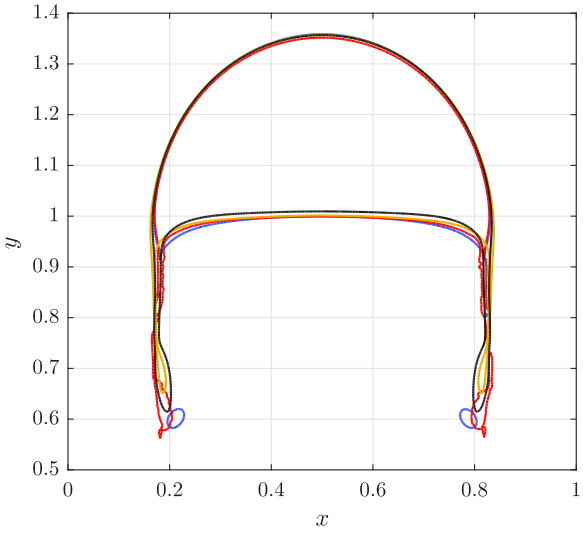

Fig. 32. Bubble shape for the rising bubble of case 2 ($Re = 35$, $Eo = 125$, $\rho_1/\rho_2 = 1000$ and $\mu_1/\mu_2 = 100$) at time $t = 3$ for $\Delta x = 1/320$ simulated with: ——, code 1; ——, code 2; ——, code 3; ——, present marker method in JADIM. (For interpretation of the references to color in this figure, the reader is referred to the web version of this article.)

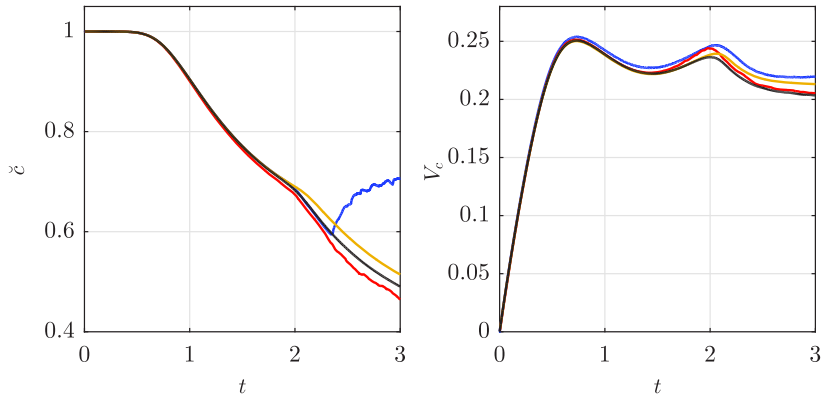

(a) Circularity (b) Centroid Position

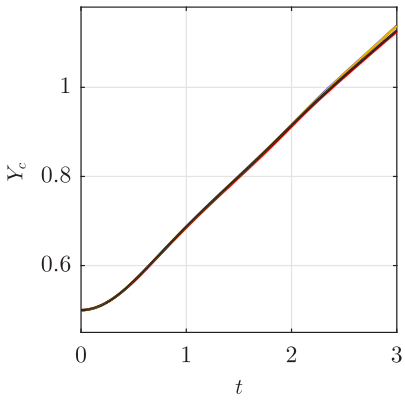

(c) Rise velocity

Fig. 33. Evolution of (a) the circularity, (b) the bubble center and (c) and the rising velocity of the 2D rising bubble of case 2 ($Re = 35$, $Eo = 125$, $\rho_1/\rho_2 = 1000$ and $\mu_1/\mu_2 = 100$) for $\Delta x = 1/320$: ——, code 1; ——, code 2; ——, code 3; ——, Present marker method in JADIM. (For interpretation of the references to color in this figure, the reader is referred to the web version of this article.)

Table 4
2D rising bubble (case 2) with $\Delta x = 1/130$. Comparison against code 1.

	e_1	e_2	e_3
Circularity $\check{c}$	3.75e−02	8.44e−02	2.16e−01
Centroid position Y_c	2.53e−03	4.15e−03	9.16e−03
Rise velocity V_c	3.29e−02	3.88e−02	6.37e−02

whose radius are taken from curvature information in the front and then are intersected with the Eulerian grid faces. The precision and stability of this reconstruction was tested and it was shown that the range $0.2 < \Delta s/\Delta x \leq 1$ provides the most accurate reconstruction given a known geometry and also provides stability in the spurious velocity reduction for both static and translating drop test cases. Also, the new reconstruction scheme was tested for a large *La* number, obtaining much better results than those obtained for the Level-Set-CSF method.

Finally, this new implementation was tested against the benchmark results proposed for a rising 2D bubble [17]. For a moderate interface deformation (Case 1), the results are independent of the frequency of reconstruction with small differences with the reference. Comparisons with the VOF-FCT-CSF and Level-Set-CSF methods implemented in JADIM show also good agreement. For the test case 2, where large deformations and break-up are present in the bubble skirt, the performance of the current implementation is comparable to those of the benchmark, specifically to code 3 not able to handle break-up as in our front method implementation. Nevertheless, the tested quantities (bubble shape, velocity and centroid position) are in very good agreement with the other codes.

Acknowledgements

Author M. Febres gratefully acknowledge financial support from FINCyT under contract 099-FINCyT-BDE-2014. Calculations were run at the computational center CALMIP (Project P1519). We would like to thank Annaïg Pedrono for the help and the support with *JADIM*.

Appendix A. Comparison against Level-Set-CSF and VOF-CSF methods

In this appendix we compare the results obtained for a rising bubble (case 1 in Table 1) with both the VOF-FCT-CSF and the Level-Set-CSF methods of JADIM [see [18,24,20]]. The volume correction [20] was not applied for the simulations reported here. The grid used for the simulation is $\Delta x = 1/320$.

The shape of the bubble at $t = 3$ is compared in Fig. A.34. The bubble shape is almost the same for the VOF-FCT-CSF, Level-Set-CSF and the present front-tracking method. A detailed inspection indicate that the Front method is closer to the Level set method. Results showing the evolution of circularity, centroid position and rise velocity are shown in Figs. A.35(a), A.35(b) and A.35(c). We see that circularity, centroid position and rise velocity are almost the same for the three methods. Circularity seems to be the more sensible quantity. A closer look to the final times, shown in Figs. A.36(a), A.36(b) and A.36(c), reveals that the present front-tracking method is closer to the Level-Set-CSF than to the VOF-FCT-CSF. This is confirmed by the differences between the present front tracking method with the Level-Set-CSF and the VOF-FCT-CSF methods shown in Tables A.5 and A.6, respectively.

Finally, we report the evolution of the mass conservation for the three methods in Fig. A.37. As indicated, the volume correction [20] was not applied for the simulations reported here for the Level-Set-CSF and the VOF-FCT-CSF. The present front tracking method appears to provide the best performances with an error around 10^{-3}% compared to 10^{-2}% and 1% for the VOF and Level Set, respectively.

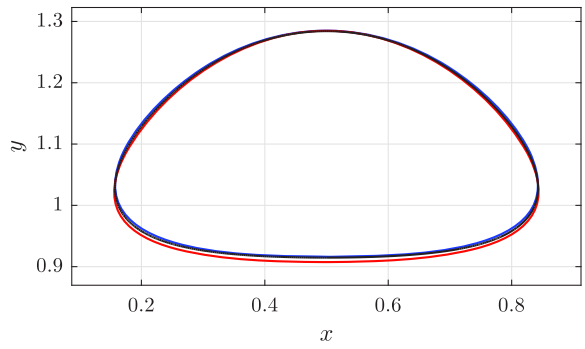

Fig. A.34. Rising Bubble shape at $t = 3$ (Case 1, Table 1). ——, Level-Set-CSF; ——, VOF-FCT; ——, Present front tracking method. (For interpretation of the references to color in this figure, the reader is referred to the web version of this article.)

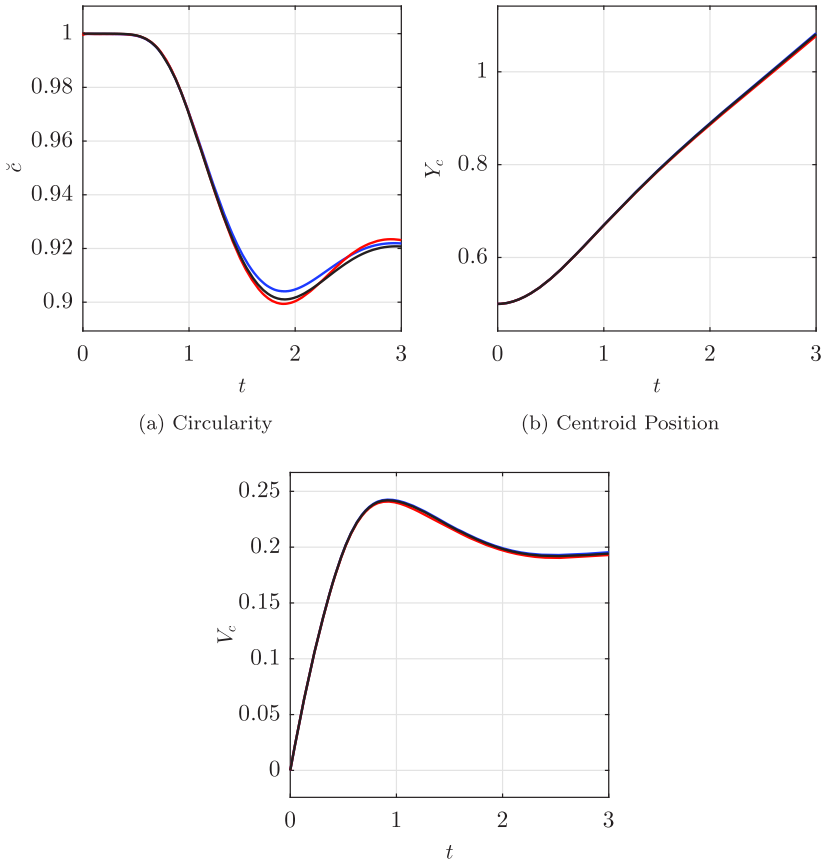

(a) Circularity (b) Centroid Position

(c) Rise velocity

Fig. A.35. Evolution of a 2D rising bubble in stagnant fluid for $\Delta x = 1/320$ (case 1). Comparison of the methods in JADIM: ——, Level-Set-CSF; ——, VOF-FCT-CSF; ——, Present front tracking method. (For interpretation of the references to color in this figure, the reader is referred to the web version of this article.)

Table A.5
Comparison for case 1 of the present front-tracking method against the Level-Set-CSF method of JADIM.

	e_1	e_2	e_3
Circularity $\check{c}$	1.46e−03	1.85e−03	3.03e−03
Centroid position Y_c	9.73e−04	1.22e−03	1.88e−03
Rise velocity V_c	3.06e−03	3.34e−03	4.83e−03

Table A.6
Comparison for case 1 of the present front-tracking with the VOF-FCT-CSF of JADIM.

	e_1	e_2	e_3
Circularity $\check{c}$	9.89e−04	1.40e−03	2.85e−03
Centroid position Y_c	1.92e−03	2.48e−03	3.68e−03
Rise velocity V_c	6.32e−03	6.87e−03	8.84e−03

Appendix B. Detailed derivation of the new tangent calculation at marker position

The derivation of the exact expression of the tangent $\boldsymbol{t}_k$ at marker k as a function of the tangent $\boldsymbol{t}_e$ and $\boldsymbol{t}_{e+1}$ of elements e and $e+1$ of length Δs_e and Δs_{e+1} is derived here (see Fig. 5). We consider than the markers positions M_{k-1}, M_k and M_{k+1} are located on the same circle in order to be consistent with the front reconstruction method. By definition minuscule vectors refer to unit vectors while majuscule vectors refers to any vector (non-necessarily with unit length).

We introduce A the point on the circle that defines the diameter AM_k. We also introduce the normal $\boldsymbol{N_z}$ of the plane $(M_{k-1}M_kM_{k+1})$ defined as

$$\boldsymbol{N_z} = \boldsymbol{t}_e \times \boldsymbol{t}_{e+1} \tag{B.1}$$

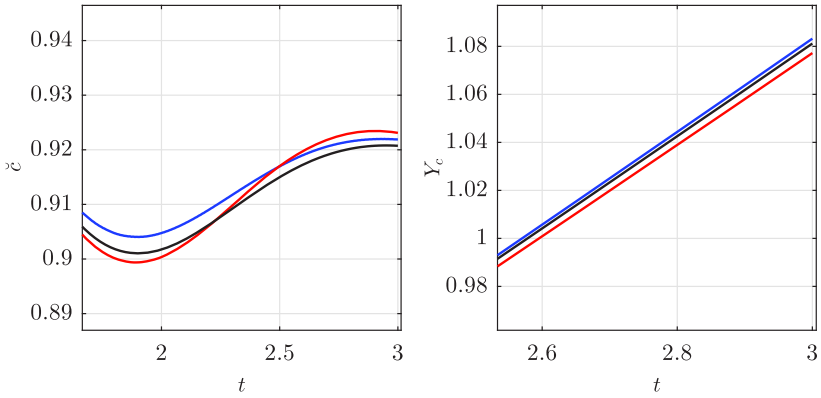

(a) Circularity (b) Centroid Position

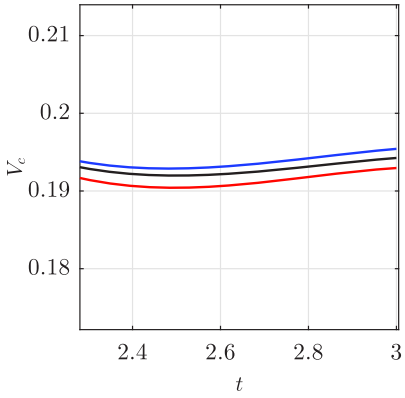

(c) Rise velocity

Fig. A.36. Evolution of a 2D rising bubble in stagnant fluid for $\Delta x = 1/320$ (case 1). Zoom of Fig. A.35. Comparison of the methods in JADIM: ——, Level-Set-CSF; ——, VOF-FCT-CSF; ——, Present front tracking method. (For interpretation of the references to color in this figure, the reader is referred to the web version of this article.)

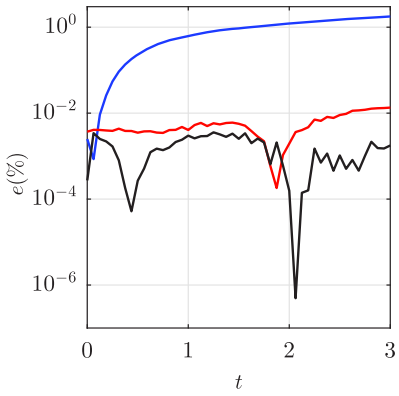

Fig. A.37. Rising Bubble shape (Case 1, Table 1). Evolution of the error in mass conservation. ——, Level-Set-CSF; ——, VOF-FCT; ——, Present front tracking method. (For interpretation of the references to color in this figure, the reader is referred to the web version of this article.)

A vector tangent to the circle at marker k can be constructed as

$$\boldsymbol{T}_k = \boldsymbol{N_z} \times \boldsymbol{AM_k} = (\boldsymbol{t}_e \times \boldsymbol{t}_{e+1}) \times \boldsymbol{AM_k} \tag{B.2}$$

giving the relation

$$\boldsymbol{T}_k = \boldsymbol{t}_{e+1}(\boldsymbol{t}_e \cdot \boldsymbol{AM_k}) - \boldsymbol{t}_e(\boldsymbol{AM_k} \cdot \boldsymbol{t}_{e+1}) \tag{B.3}$$

Replacing $\boldsymbol{AM_k}$ by $\boldsymbol{AM_{k-1}} + \Delta s_e \boldsymbol{t}_e$ in the first term and by $\boldsymbol{AM_{k+1}} - \Delta s_{e+1} \boldsymbol{t}_{e+1}$ in the second term and noting that $\boldsymbol{t}_e$ (resp. $\boldsymbol{t}_{e+1}$) is orthogonal with $\boldsymbol{AM_{k-1}}$ (resp. $\boldsymbol{AM_{k+1}}$), it follows

$$\boldsymbol{T}_k = \Delta s_{e+1} \boldsymbol{t}_e + \Delta s_e \boldsymbol{t}_{e+1} \tag{B.4}$$

The unit vector $\boldsymbol{t}_k$ used for the capillary force calculation is then deduced from $\boldsymbol{T}_k$:

$$\boldsymbol{t}_k = \frac{\Delta s_{e+1} \boldsymbol{t}_e + \Delta s_e \boldsymbol{t}_{e+1}}{\sqrt{\Delta s_{e+1}^2 + \Delta s_e^2 + 2 \Delta s_{e+1} \Delta s_e \boldsymbol{t}_e \cdot \boldsymbol{t}_{e+1}}} \tag{B.5}$$

References

[1] S.H. Garrioch, B.R. Baliga, A PLIC volume tracking method for the simulation of two-fluid flows, Int. J. Numer. Methods Fluids 52 (10) (2006) 1093–1134, https://doi.org/10.1002/fld.1217.

[2] C. Hirt, B. Nichols, Volume of fluid (VOF) method for the dynamics of free boundaries, J. Comput. Phys. 39 (1) (1981) 201–225, https://doi.org/10.1016/0021-9991(81)90145-5, http://www.sciencedirect.com/science/article/pii/0021999181901455.

[3] M. Rudman, Volume-tracking methods for interfacial flow calculations, Int. J. Numer. Methods Fluids 24 (7) (1997) 671–691, https://doi.org/10.1002/(SICI)1097-0363(19970415)24:7<671::AID-FLD508>3.0.CO;2-9.

[4] M. Sussman, P. Smereka, S. Osher, A level set approach for computing solutions to incompressible two-phase flow, J. Comput. Phys. 114 (1) (1994) 146–159, https://doi.org/10.1006/jcph.1994.1155, http://www.sciencedirect.com/science/article/pii/S0021999184711557.

[5] Y. Chang, T. Hou, B. Merriman, S. Osher, A level set formulation of eulerian interface capturing methods for incompressible fluid flows, J. Comput. Phys. 124 (2) (1996) 449–464, https://doi.org/10.1006/jcph.1996.0072, http://www.sciencedirect.com/science/article/pii/S0021999196900728.

[6] S.P. van der Pijl, A. Segal, C. Vuik, P. Wesseling, A mass-conserving level-set method for modelling of multi-phase flows, Int. J. Numer. Methods Fluids 47 (4) (2005) 339–361, https://doi.org/10.1002/fld.817.

[7] S. Shin, S. Abdel-Khalik, V. Daru, D. Juric, Accurate representation of surface tension using the level contour reconstruction method, J. Comput. Phys. 203 (2) (2005) 493–516, https://doi.org/10.1016/j.jcp.2004.09.003, http://www.sciencedirect.com/science/article/pii/S0021999104003894.

[8] G. Tryggvason, B. Bunner, A. Esmaeeli, D. Juric, N. Al-Rawahi, W. Tauber, J. Han, S. Nas, Y.-J. Jan, A front-tracking method for the computations of multiphase flow, J. Comput. Phys. 169 (2001) 708–759, https://doi.org/10.1006/jcph.2001.6726.

[9] S. Popinet, S. Zaleski, A front-tracking algorithm for accurate representation of surface tension, Int. J. Numer. Methods Fluids 30 (1999) 775–793, https://doi.org/10.1002/(SICI)1097-0363(19990730)30:6<775::AID-FLD864>3.3.CO;2-R.

[10] T.Y. Hou, J.S. Lowengrub, M.J. Shelley, Removing the stiffness from interfacial flows with surface tension, J. Comput. Phys. 114 (2) (1994) 312–338, https://doi.org/10.1006/jcph.1994.1170, http://www.sciencedirect.com/science/article/pii/S0021999184711703.

[11] S.O. Unverdi, G. Tryggvason, A front-tracking method for viscous, incompressible, multi-fluid flows, J. Comput. Phys. 100 (1992) 25–37, https://doi.org/10.1016/0021-9991(92)90307-K.

[12] D. Juric, G. Tryggvason, Computations of boiling flows, Int. J. Multiph. Flow 24 (3) (1998) 387–410, https://doi.org/10.1016/S0301-9322(97)00050-5, http://www.sciencedirect.com/science/article/pii/S0301932297000505.

[13] C.-Y.H. Ming-Chih Lai, Y.-M. Huang, Simulating the axisymmetric interfacial flows with insoluble surfactant by immersed boundary method, Int. J. Numer. Anal. Model. 8 (1) (2011) 105–117.

[14] M.S. Longuet-Higgins, E.D. Cokelet, The deformation of steep surface waves on water. I. A numerical method of computation, Proc. R. Soc. Lond. A, Math. Phys. Eng. Sci. 350 (1660) (1976) 1–26, https://doi.org/10.1098/rspa.1976.0092, arXiv: http://rspa.royalsocietypublishing.org/content/350/1660/1.full.pdf, http://rspa.royalsocietypublishing.org/content/350/1660/1.

[15] H.D. Ceniceros, A.M. Roma, A multi-phase flow method with a fast, geometry-based fluid indicator, J. Comput. Phys. 205 (2) (2005) 391–400, https://doi.org/10.1016/j.jcp.2004.11.013, http://www.sciencedirect.com/science/article/pii/S0021999104004759.

[16] A. Savitzky, M.J.E. Golay, Smoothing and differentiation of data by simplified least squares procedures, Anal. Chem. 36 (8) (1964) 1627–1639, https://doi.org/10.1021/ac60214a047.

[17] S. Hysing, S. Turek, D. Kuzmin, N. Parolini, E. Burman, S. Ganesan, L. Tobiska, Quantitative benchmark computations of two-dimensional bubble dynamics, Int. J. Numer. Methods Fluids 60 (11) (2009) 1259–1288, https://doi.org/10.1002/fld.1934.

[18] T. Bonometti, J. Magnaudet, An interface-capturing method for incompressible two-phase flows. Validation and application to bubble dynamics, Int. J. Multiph. Flow 33 (2) (2007) 109–133, https://doi.org/10.1016/j.ijmultiphaseflow.2006.07.003, http://www.sciencedirect.com/science/article/pii/S0301932206001315.

[19] J.-B. Dupont, D. Legendre, Numerical simulation of static and sliding drop with contact angle hysteresis, J. Comput. Phys. 229 (7) (2010) 2453–2478, https://doi.org/10.1016/j.jcp.2009.07.034, http://www.sciencedirect.com/science/article/pii/S0021999109004203.

[20] T. Abadie, J. Aubin, D. Legendre, On the combined effects of surface tension force calculation and interface advection on spurious currents within volume of fluid and level set frameworks, J. Comput. Phys. 297 (2015) 611–636, https://doi.org/10.1016/j.jcp.2015.04.054, http://www.sciencedirect.com/science/article/pii/S0021999115003113.

[21] D. Legendre, M. Maglio, Numerical simulation of spreading drops, Colloids Surf. A, Physicochem. Eng. Asp. 432 (2013) 29–37, https://doi.org/10.1016/j.colsurfa.2013.04.046, http://www.sciencedirect.com/science/article/pii/S0927775713003415.

[22] D. Legendre, M. Maglio, Comparison between numerical models for the simulation of moving contact lines, small scale simulation of multiphase flows, Comput. Fluids 113 (2015) 2–13, https://doi.org/10.1016/j.compfluid.2014.09.018, http://www.sciencedirect.com/science/article/pii/S0045793014003557.

[23] J. Brackbill, D. Kothe, C. Zemach, A continuum method for modeling surface tension, J. Comput. Phys. 100 (2) (1992) 335–354, https://doi.org/10.1016/0021-9991(92)90240-Y, http://www.sciencedirect.com/science/article/pii/002199919290240Y.

[24] T. Abadie, Hydrodynamics of Gas–Liquid Taylor Flow in Microchannels, Ph.D. thesis, Institut National Polytechnique de Toulouse, INP Toulouse, 2013.

[25] H.D. Ceniceros, A.M. Roma, A. Silveira-Neto, M.M. Villar, A robust, fully adaptive hybrid level-set/front-tracking method for two-phase flows with an accurate surface tension computation, Commun. Comput. Phys. 8 (2010) 51–94, https://doi.org/10.4208/cicp.050509.141009a.

[26] G. Agresar, J. Linderman, G. Tryggvason, K. Powell, An adaptive, cartesian, front-tracking method for the motion, deformation and adhesion of circulating cells, J. Comput. Phys. 143 (2) (1998) 346–380, https://doi.org/10.1006/jcph.1998.5967, http://www.sciencedirect.com/science/article/pii/S0021999198959678.

[27] Y. Yamamoto, T. Uemura, Numerical experiment of drop spreading by front-tracking method, J. Jap. Soc. Exp. Mech. 8 (Special Issue) (2008) s43–s48, https://doi.org/10.11395/jjsem.8.s43.

[28] Y. Yamamoto, T. Ito, T. Wakimoto, K. Katoh, Numerical simulations of spontaneous capillary rises with very low capillary numbers using a front-tracking method combined with generalized Navier boundary condition, Int. J. Multiph. Flow 51 (2013) 22–32, https://doi.org/10.1016/j.ijmultiphaseflow.2012.12.002, http://www.sciencedirect.com/science/article/pii/S0301932212001759.

[29] Y. Yamamoto, K. Tokieda, T. Wakimoto, T. Ito, K. Katoh, Modeling of the dynamic wetting behavior in a capillary tube considering the macroscopic–microscopic contact angle relation and generalized Navier boundary condition, Int. J. Multiph. Flow 59 (2014) 106–112, https://doi.org/10.1016/j.ijmultiphaseflow.2013.10.018, http://www.sciencedirect.com/science/article/pii/S0301932213001699.
[30] S. Shin, D. Juric, Modeling three-dimensional multiphase flow using a level contour reconstruction method for front tracking without connectivity, J. Comput. Phys. 180 (2) (2002) 427–470, https://doi.org/10.1006/jcph.2002.7086, http://www.sciencedirect.com/science/article/pii/S0021999102970865.
[31] M.-C. Lai, Y.-H. Tsend, H. Huang, Numerical simulation of moving contact lines with surfactant by immersed boundary method, Commun. Comput. Phys. 8 (2010) 735–757, https://doi.org/10.4208/cicp.281009.120210a.
[32] H. Huang, D. Liang, B. Wetton, Computation of a moving drop/bubble on a solid surface using a front-tracking method, Commun. Math. Sci. 2 (4) (2004) 535–552, http://projecteuclid.org/euclid.cms/1109885497.
[33] Y. Li, E. Jung, W. Lee, H.G. Lee, J. Kim, Volume preserving immersed boundary methods for two-phase fluid flows, Int. J. Numer. Methods Fluids 69 (4) (2012) 842–858, https://doi.org/10.1002/fld.2616.
[34] C.S. Peskin, The immersed boundary method, Acta Numer. 11 (2002) 479–517, https://doi.org/10.1017/S0962492902000077, https://www.cambridge.org/core/article/immersed-boundary-method/95ECDAC5D1824285563270D6DD70DA9A.
[35] S. Popinet, An accurate adaptive solver for surface-tension-driven interfacial flows, J. Comput. Phys. 228 (16) (2009) 5838–5866, https://doi.org/10.1016/j.jcp.2009.04.042.
[36] D. Torres, J. Brackbill, The point-set method: front-tracking without connectivity, J. Comput. Phys. 165 (2) (2000) 620–644, https://doi.org/10.1006/jcph.2000.6635, http://www.sciencedirect.com/science/article/pii/S002199910096635X.
[37] R. Scardovelli, S. Zaleski, Direct numerical simulation of free-surface and interfacial flow, Annu. Rev. Fluid Mech. 31 (1999) 567–603, https://doi.org/10.1146/annurev.fluid.31.1.567.